Journal of Nanobiotechnology

RESEARCH

Open Access

NUP85 siRNA loaded red blood cell-derived extracellular vesicles alleviate hepatic steatosis in MASLD

Zhuan Zhang[1,2], Shihui Li[1], Yu Zhang[1,2], Ruizi Xu[1,2], Jing Zhou[1,3], Yanan Wang[4] and Yongmin Yan[1,3*]

Abstract

Metabolic Dysfunction-Associated Steatotic Liver Disease (MASLD) is the most prevalent chronic liver disease globally; however, it currently lacks sensitive and specific non-invasive diagnostic biomarkers, as well as safe and effective targeted therapies. In this study, we investigate the diagnostic and therapeutic potential of Nucleoporin 85 (NUP85) and successfully develop an innovative targeted delivery system. Our findings reveal that serum NUP85 levels are significantly elevated in MASLD patients and positively correlate with disease severity. Serum NUP85 demonstrates exceptional diagnostic performance in differentiating Metabolic Dysfunction-Associated Steatohepatitis (MASH) from cirrhosis, significantly outperforming traditional liver function indicators. Additionally, we have developed a siNUP85 delivery system utilizing red blood cell-derived extracellular vesicles (RBC-EVs). The RBC-EVs@siNUP85 exhibits excellent biocompatibility and liver-targeting capability, facilitating the efficient delivery of siNUP85 to hepatocytes. Both in vitro and in vivo experiments confirm that RBC-EVs@siNUP85 can effectively silence NUP85 expression in the liver, significantly alleviating hepatic steatosis, inflammatory responses, and oxidative stress, while restoring liver function without notable toxic side effects. Mechanistic studies indicate that NUP85 is significantly upregulated in lipotoxic hepatocytes in high-fat diet (HFD) or methionine-choline-deficient (MCD) diet mice. NUP85 promotes lipid accumulation in lipotoxic hepatocytes by modulating the solute carrier family 27 member 1 (SLC27A1)/PPAR-γ signaling pathway, thereby enhancing the expression of lipid synthesis-related genes and inflammatory factors.

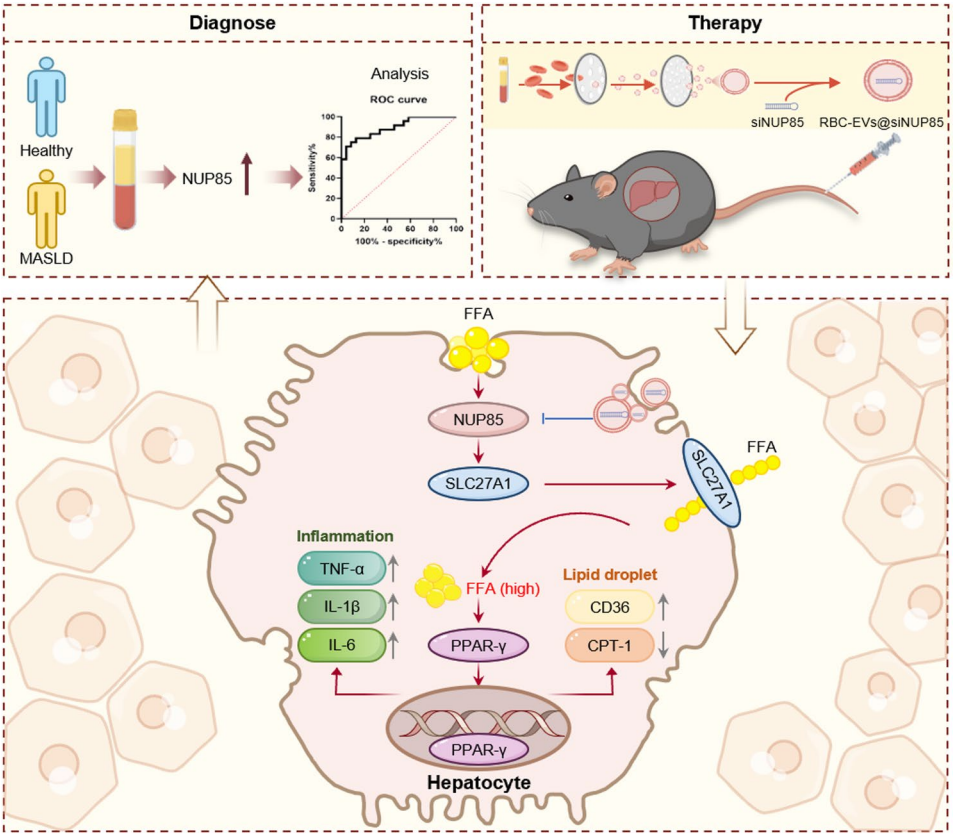
Keywords NUP85, Diagnose, Lipid deposition, MASLD, SLC27A1, PPAR-γ, RBC-EVs

*Correspondence:
Yongmin Yan
yym@ujs.edu.cn

Full list of author information is available at the end of the article

© The Author(s) 2025. **Open Access** This article is licensed under a Creative Commons Attribution-NonCommercial-NoDerivatives 4.0 International License, which permits any non-commercial use, sharing, distribution and reproduction in any medium or format, as long as you give appropriate credit to the original author(s) and the source, provide a link to the Creative Commons licence, and indicate if you modified the licensed material. You do not have permission under this licence to share adapted material derived from this article or parts of it. The images or other third party material in this article are included in the article's Creative Commons licence, unless indicated otherwise in a credit line to the material. If material is not included in the article's Creative Commons licence and your intended use is not permitted by statutory regulation or exceeds the permitted use, you will need to obtain permission directly from the copyright holder. To view a copy of this licence, visit http://creativecommons.org/licenses/by-nc-nd/4.0/.

Graphical abstract



Introduction

Metabolic dysfunction-associated fatty liver disease (MASLD) represents a significant global health concern, characterized by a diverse array of symptoms [1]. MASLD encompasses metabolic dysfunction-related steatohepatitis, liver fibrosis, cirrhosis, and hepatocellular carcinoma, and is closely associated with risk factors such as type 2 diabetes (T2D), obesity, cardiovascular complications, and metabolic syndrome [2]. The excessive accumulation of lipids within hepatocytes serves as a crucial driving factor in the progression of MASLD [3]. While various pharmacological treatments for obesity and T2D are currently available to address their comorbidities [4], they do not adequately fulfill clinical needs, and there is no ideal non-invasive diagnostic marker [5]. Consequently, there is an urgent need to investigate the molecular mechanisms by which excessive lipid deposition contributes to the progression of MASLD, identify specific non-invasive biomarkers, and develop novel treatment strategies for this condition.

Nuclear pore complexes (NPCs) are macromolecular structures embedded in the nuclear membrane [6]. Nucleoporin 85 (NUP85), a component of the nuclear pore complex Y complex (NUP107-160 complex), is essential for regulating nucleocytoplasmic transport, mitosis, and transcription [7]. Mutations in several nucleoporin genes have been linked to a range of human diseases [8]. Research indicates that NUP85 influences tumor-associated macrophage responses and facilitates tumor progression [9]. Additionally, a separate study demonstrated that NUP85 interacts with chemokine receptors, mediating the recruitment of monocytes and thereby promoting liver inflammation and disease progression [10]. Various factors, including lipid deposition and inflammatory responses, can induce MASLD-related oxidative stress, mitophagy, endoplasmic reticulum stress, and other reactions [11–13]. When these responses become imbalanced, the damaged liver releases various signals to repair these pathological changes, which in turn exacerbates and amplifies lipid accumulation and inflammation. The critical role of NUP85 in MASLD-related lipid deposition, along with its potential implications for diagnosis and treatment, requires further investigation [14].

Several studies have demonstrated that the targeted delivery of small interfering RNA (siRNA) serves as an effective treatment for various diseases, including acute lung injury (ALI) [15], acute kidney injury [16], breast

cancer [17], pancreatic cancer [18], and metabolic dysfunction-associated steatotic liver disease (MASLD) [19]. Consequently, the siRNA delivery of NUP85 is anticipated to emerge as a novel strategy for treating MASLD. Nonetheless, the development of safe and effective siRNA delivery systems remains a significant challenge [20]. RBC-EVs may present a promising delivery vector. Utilizing RBC-EVs as carriers can facilitate the targeted delivery of miR-214 to osteoclasts for the treatment of osteoporosis [21]. In a mouse model of cancer cachexia, employing RBC-EVs to deliver Mstn siRNA to skeletal muscle resulted in reduced muscle loss and prolonged survival of the mice [22]. However, the potential of RBC-EVs as liver-targeted siRNA drug carriers in the treatment of MASLD remains uncertain.

In summary, this study demonstrates that RBC-EVs deliver si*Nup85*, which alleviates MASLD by downregulating SLC27A1/PPAR-γ in hepatocytes. Furthermore, NUP85 holds significant potential for the diagnosis of MASLD patients. First, this study assessed the serum levels of NUP85 in peripheral blood samples from patients with MASLD, establishing the diagnostic efficacy of serum NUP85 for this condition. Second, the research investigates the relationship between NUP85 and lipid accumulation and deposition in MASLD, clarifying the potential mechanisms through which NUP85 facilitates lipid deposition in hepatocytes. Specifically, NUP85 interacts with SLC27A1 to modulate the PPAR-γ signaling pathway, thereby impacting lipid metabolism. Lastly, the targeted inhibition of NUP85 expression in mouse liver via RBC-EVs delivering siNUP85 presents a novel approach for the treatment of MASLD.

Materials and methods

Cell culture

Human liver hepatocellular carcinoma cell line HepG2 and mouse hepatocyte line AML12 utilized in this study were obtained from the Chinese Academy of Sciences (Shanghai, China). Mouse primary hepatocytes (MPH) were isolated from C57BL/6 mice. HepG2 were cultured in high-glucose DMEM medium (Cytiva, China, SH30243.01) supplemented with 10% FBS (Excell Bio, China, FSS500). AML12 were maintained in DMEM medium (Gibco, USA, 11885084) also containing 10% FBS. MPH were cultured in DMEM/F12 medium (Viva-Cell, China, C3132) with 10% FBS. All cell lines were incubated at 37℃ in a humidified atmosphere with 5% CO_2. Each cell line was authenticated by STR analysis and confirmed to be mycoplasma-free using the Myco-Lumi™ Luminescent Mycoplasma Detection Kit (Beyotime, China, C0297S).

Table 1 Antibodies used in Western blot

Antibody	Dilution	Supplier	Reference
Anti-NUP85	1:500	Santa Cruz	sc-376,111
Anti-SLC27A1	1:1000	Abclonal	A-12,847
Anti-PPAR-γ	1:1000	AiFang	AF03097
Anti-β-actin	1:2000	Abclonal	AC026
Anti-GAPDH	1:2000	Abclonal	AC001
HRP Goat Anti-rabbit IgG(H + L)	1:2000	Abclonal	AS014
HRP Goat Anti-mouse IgG(H + L)	1:2000	Abclonal	AS003

Western blot

Protein was extracted from HepG2, AML12, MPH, mouse liver tissue, and RBC-EVs using RIPA buffer (Beyotime, China, P0013B) supplemented with 1 mM phenylmethylsulfonyl fluoride (PMSF) (Biosharp, China, BL507A). The concentration of protein samples was measured by a BCA protein assay kit (CWBIO, China, CW0014S). Protein was separated in 10% SDS-PAGE denaturing gel and subsequently transferred to the PVDF membrane. The membrane was then blocked with 5% milk at room temperature for 2 h. Following this, the membrane was incubated with the appropriate primary antibody overnight at 4℃. Then, HRP-conjugated secondary antibodies were applied at room temperature for 2 h. Immune complexes were visualized and analyzed using the Chemi-Doc system (Tanon, Shanghai, China) along with enhanced chemiluminescence detection reagent (Tanon, China, 180–5001), and quantified using ImageJ software. Relative expression levels were normalized to the expression of β-actin or GAPDH. Details regarding the antibodies used are provided in Table 1.

Immunohistochemistry staining

First, the paraffin sections of liver were dewaxed and dehydrated. Then the liver sections were soaked in citrate buffer and heated at 100℃ for 30 min. The endogenous peroxidase was then inactivated by 3% H_2O_2. Following this, the sections were blocked with 5% BSA and incubated overnight at 4℃ with the primary antibody against NUP85. The slices were then incubated with the corresponding secondary antibody (Biotin-coupled goat anti-mouse/rabbit IgG) and SABC (Strept Avidin-Biotin Complex). Then, liver tissue sections were visualized with DAB Horseradish Peroxidase Color Development Kit (Boster, Wuhan, AR1025). Finally, the nucleus was stained with hematoxylin dye solution. Images were obtained using a pathological section scanner (3DHISTECH, Hungary).

Quantitative reverse transcription PCR (qRT-PCR)

Using Trizol reagent (Invitrogen, USA, 15596018CN) and the manufacturer's instructions, the total RNA was isolated from cultured cells and liver tissues. And 1 mg RNA was reverse-transcribed to cDNA using HiScript® lll 1 st Strand cDNA Synthesis Kit (+ gDNA wiper) (Vazyme, China, R312-02). When conducting real-time PCR,

Table 2 Primer sequences used in RT-qRCR for human

Gene	Forward 5′–3′	Reverse 5′–3′
ACTB	GGCCAACCGCGAGAAGATGAC	GGATAGCACAGCCTGGATAGCAAC
NUP85	CGCGAGTTCCACCGTATGTA	CTCCAGACACCGCATCAACT
SLC27A1	ATGGCTATGTCAGCGAGAGC	TACCCTCCACTCCTGGAACA
SREBP1	GCTGTCCACAAAAGCAAATCTC	GTCAGTGTGTCCTCCACCTCAGT
ACC1	CTTCCTGCTCATACACTTCT	GTATAACTGCTGCCATCATAG
FASN	TTCTACGGCTCCACGCTCTTCC	GAAGAGTCTTCGTCAGCCAGGA
PPARA	ACTTATCCTGTGGTCCCCGG	CCGACAGAAAGGCACTTGTGA
CPT1	AAGTTGGCGTCTGAGAAG	GGTCTGGCTTGTTGATAATC
CPT2	ACAGTGCTGGTGAGCTTCAG	TCAAAGCCCTGGCCCATTG
LCAD	TTTGGGAGGACACCACAGG	CCAGCTTTCTCCCATTCTGAGT
TNF	GCCCATGTTGTAGCAAACCC	TGAGGTACAGGCCCTCTGAT
IL1B	AACCTCTTCGAGGCACAAGG	GTCCTGGAAGGAGCACTTCAT
IL6	TTCTCCACAAGCGCCTTC	TTCTCCACAAGCGCCTTC
TGFB1	TGATGTCACCGGAGTTGTGC	CGGTAGTGAACCCGTTGATG
FATP2	CTGGTGTCGCCAGAACTACA	GGCAAGAGTAGCACCTGTGG
FATP3	CCCTGCTGGAATTAGCGATTT	GGGCGAGGTAGATCACATCTT
FATP4	CGGCTAAACCCTGCTGAGAC	GACCAGGCCGCCAAAGATA
CD36	AAGGAAAATGTAACCCAGGACG	CAGCCAGATTGAGAACTGTGAAG
PPARG	AGAGCCTTCCAACTCCCTCA	AAACCCTTGCATCCTTCACA

Table 3 Primer sequences used in RT-qRCR for mouse

Gene	Forward 5′–3′	Reverse 5′–3′
Actb	AACAGTCCGCCTAGAAGCAC	CGTTGACATCCGTAAAGACC
Nup85	GAGCCCGCAGTAACTTGGAT	GCTCGGCACCTTCTCTGATT
Il-1b	GAAATGCCACCTTTTGACAGTG	TGGATGCTCTCATCAGGACAG
Il6	ACAAAGCCAGAGTCCTTCAGAG	CATTGGAAATTGGGGTAGGA
Tnf	GTCTACTGAACTTCGGGGTGAT	ATGATCTGAGTGTGAGGGTCTG
Tgfb1	CTCCCGTGGCTTCTAGTGC	GCCTTAGTTTGGACAGGATCTG
Col1a1	CACCCCAATCTGGTTCCCTC	CATAAGCCAAGTGGGCAGGA
Col3a1	CTGGTCAGCCTGGAGATAAG	ACCAGGACTACCACGTTCAC
Acta2	GTACCCAGGCATTGCTGACA	GAGGCGCTGATCCACAAAAC

quantitative measurements were taken using the ChamQ SYBR Color qPCR Master Mix (Vazyme, China, Q312-02) and the ABI Prism 2720 PCR system (Applied Biosystems, USA). Genomic expression levels were determined by normalizing the ratio of each control to the total number of units, with β-actin as the reference. The following primers were used (Tables 2 and 3).

H&E staining

The paraffin sections of mouse liver tissues were dewaxed and stained with hematoxylin and eosin (H&E) dye. The pathological changes of liver tissues in each group were observed.

Table 4 Primary antibodies for Immunofluorescence staining

Antibody	Dilution	Supplier	Reference
Anti-NUP85	1:50	Santa Cruz	sc-376,111
Anti-SLC27A1	1:100	Abclonal	A-12,847
Anti-Albumin	1:100	Santa Cruz	sc-271,605
Anti-F4/80	1:100	Santa Cruz	sc-377,009
Anti-α-SMA	1:100	Santa Cruz	sc-53,142
Anti-β-actin	1:200	Abclonal	AC026
FITC Goat Anti-Rabbit IgG (H + L)	1:200	Abclonal	AS011
Cy3 Goat Anti-Mouse IgG (H + L)	1:200	Abclonal	AS008

Human serum samples

The blood samples were collected after obtaining informed consent from 120 MASH patients and 110 cirrhosis patients, and 100 healthy volunteers were used as age and sex-matched control groups collected from the Third People's Hospital of Changzhou, China. The blood samples were centrifuged, and serum was isolated and kept at −80℃ until analysis. Informed consent was given to all patients examined. All samples were confirmed by pathological examination. Histological grade was defined according to the World Health Organization classification. Documented informed consent was obtained from all subjects, and the Ethics Committee of Wujin People's Hospital in Changzhou, Jiangsu Province, approved all aspects of the study (2025-SR-019). Characteristics of male and female MASH and cirrhosis patients used in this study at Table S1 and Table S2.

Determination of serum NUP85 concentration

The serum NUP85 concentration was measured in both patients and controls using commercial ELISA kits (Shanghai Jianglai Biotechnology Co., Ltd, China, JL36597). Following the manufacturer's instructions, we added 100 μL of serum and standard solution to a 96-well microplate coated with capture antibody, plus biotinylated antibody and enzyme conjugate to form a complex, referring to the instructions. Finally, the TMB substrate was added and the concentration of NUP85 was calculated by detecting the absorbance at 450 nm using an enzyme-linked immunoassay instrument.

Immunofluorescence staining

According to the immunohistochemistry method described, liver slices were preprocessed and incubated with primary antibodies overnight at 4℃. Following this, the slices were incubated with secondary antibodies and washed three times with PBS. Cell nuclei were stained using Hoechst dye. For cell samples, HepG2, AML12, and MPH cells were washed three times with PBS, fixed with 4% paraformaldehyde for 20 min, and permeabilized with

0.1% Triton X-100 (Beyotime, China, P0096). The cells were then blocked with 5% BSA for 1 h, incubated with primary antibodies overnight at 4℃, and subsequently incubated with secondary antibodies for 1 h at room temperature in the dark. Cell nuclei were also stained with Hoechst dye (Beyotime, China, C1025). Images were captured using a fluorescence microscope and quantified with ImageJ. The following antibodies were used (Table 4).

BODIPY 493/503 staining

After the cells were fixed according to the above-mentioned immunofluorescence staining method, BODIPY 493/503 kit (Beyotime, China, C2053S) was used for staining. The images were captured by fluorescence microscope and quantified by ImageJ.

Oil red O staining

Oil Red O (Sigma, USA, 1320-06–5) was dissolved in 100% isopropanol to prepare a reserve solution. A working solution was then made by diluting the Oil Red O solution with distilled water in a 3:2 ratio, followed by filtration through a 0.2 μm filter. Cells in the 24-well plate or fast-frozen liver sections were washed with PBS and fixed with 4% paraformaldehyde (Solarbio, UK, P1110) at room temperature for 30 min. After fixation, the cells were washed again with PBS and incubated with 60% isopropanol for 3 min. Subsequently, the cells were stained with the Oil Red O solution at room temperature for 20 min, and the color was adjusted using 60% isopropanol. Finally, the nuclei were stained with hematoxylin dye, and images of the lipid droplets in the stained cells were observed under a microscope.

Biochemical analysis

Initially, isopropyl alcohol was added to adherent HepG2 cultures, followed by homogenization. The supernatant was subsequently collected after centrifugation at 12,000 × g for 5 min at 4℃. The levels of triglycerides (TG) and free fatty acids (FFA) in the cells were measured using a commercial kit. Serum levels of triglycerides (TG), free fatty acids (FFA), total cholesterol (TC), alanine aminotransferase (ALT), and aspartate aminotransferase (AST) in both humans and mice were analyzed according to the manufacturers' instructions using a MINDRAY BS200 chemistry analyzer (MINDRAY Medical International Co., Shenzhen, China).

ROS content

For assessing the total intracellular levels of reactive oxygen species (ROS) in HepG2 or AML12, the cells were washed three times with phosphate-buffered saline (PBS) and then incubated with either DHE working solution or DCFH-DA probe at 37℃ in an atmosphere of 5% CO2 for 30 min. The DHE staining data analysis was performed using ImageJ software.

MDA, SOD and GSH level

The levels of MDA (Beyotime, China, S0131S), GSH (Nanjing Jiancheng Bioengineering Institute, Nanjing, China, A006-2-1), and SOD (Beyotime, China, S0101S) were measured using commercial kits. These procedures were performed according to the protocol provided by the reagent manufacturer.

Cell viability assay

HepG2 and AML12 cells were seeded into 96-well cell culture plates and treated with either RBC-EVs@siNC or RBC-EVs@siNUP85 for 24 h. The medium was then replaced with complete culture medium. Then 10 μl CCK-8 solution (Biosharp, China, BS350A) was added to each well. Next, the cells were incubated at 37℃ with 5% CO2 for 1 h. Cell viability was monitored continuously for 3 days by measuring absorbance at 450 nm using an enzyme-labeled instrument. All experiments were performed in triplicate.

Protein interaction network construction

The STRING database (https://string-db.org/) was used to construct a protein-protein interaction (PPI) network to analyze and identify protein interactions. First, we searched for interacting proteins for NUP85, with the required minimum interaction score set to 0.4 (medium confidence) to ensure biologically meaningful interactions while maintaining network connectivity, and the organism set to "Homo sapiens", resulting in a total of 240 interacting proteins. We then screened the predicted interacting proteins for proteins associated with lipid deposition and metabolism, including SLC27A1, which has a direct interaction with NUP85. Finally, we selected several proteins that interact closely with NUP85 and SLC27A1, respectively, and constructed a protein-protein interaction network by inputting multiple protein names into "Multiple proteins".

NUP85-related transcriptome data retrieval

Data sets containing transcriptome profiling data related to "MASLD" or "NUP85" were acquired from the GEO database (GSE135251 and GSE167523). According to Article 32 in Chap. 3 of the "Ethical Review Measures for Life Science and Medical Research Involving Human Subjects" issued by the National Science and Technology Ethics Committee of China, the use of legally obtained publicly available personal information data or biological samples for life science and medical research can be exempted from ethical review.

Extraction of red blood cell-derived extracellular vesicles (RBC-EVs)

First, we collected peripheral blood from type O donors. Then, RBCs were separated from plasma and white blood cells by centrifugation at 2,000 × g for 10 min, the isolated RBCs were resuspended in PBS. Then, the RBCs suspension was sequentially extruded 4 times through 5 μm and 1 μm polycarbonate membrane filters using a mini extruder (Avanti Polar Lipids, USA). To enrich RBC-EVs, the extruded samples were ultracentrifuged at 100,000 × g for 70 min at 4℃. Finally, the purified RBC-EVs were dissolved with PBS and stored at −80℃ until use. The protein content of the EVs was quantified using a detergent-free BCA Protein Assay Kit (Thermo Fisher Scientific, CA).

Nanoparticle tracking analysis

Nanoparticle tracking analysis was used to measure the number and size of RBC-EVs. The system used was a NanoSightNS500 (Malvern, UK). Polystyrene beads, of 100 nm, were used to calibrate the instrument (Thermo Fisher Scientific, CA) before use. For recordings, samples were pumped automatically into a chamber at a constant flow rate using the Malvern NanoSight syringe pump system. The camera level was adjusted to 11, and three 60 s captures per sample were recorded. For analysis of the recordings, the detection threshold was set to 5, and the NTA 3.3 Suite Software was used for analysis.

Transmission electron microscopy

RBC-EVs were diluted in PBS and placed on 200-mesh carbon-coated copper grids at room temperature for 5 min. The excess suspension was removed using filter paper. Then, the RBC-EVs were negatively stained with 0.75% uranyl acetate at room temperature for 5 min, washed twice with PBS, dried and examined under an FEI Tecnai T10 electron microscope (FEI, Hillsboro, OR, USA) operating at 100 kV.

NUP85 siRNA loading into RBC-EVs by electroporation

In this study, two siRNAs for NUP85 were designed and synthesized (synthesized and provided by Genepharma, China). The sense strand of the Mus-*Nup85* siRNA was 5'-GGCCUUUGAGUUCGACAUUTT-3', the antisense strand was 5'-AAUGUCGAACUCAAAGGCCTT-3'; The sense strand of the Homo-*NUP85* siRNA was 5'-GG AGAUGCUGGUAUGUGAATT-3', the antisense strand was 5'-UUCACAUACCAGCAUCUCCTT-3'. Negative control FAM and negative control siRNA were purchased from Genepharma Biotechnology Co., Ltd. Firstly, 5 μg siRNA-*NUP85*, siRNA-*Nup85*, siRNA-FAM or siRNA-NC and 45 μL RBC-EVs (10^{11} particles/mL) were lightly mixed and electroporated in a 4 mm cuvette by the electroporation apparatus using a 0.35 s pulse 2 times at 0.7 kV as previously described. Then, we incubated the mixture at 37℃ for 2 h to recover the complete membrane structure. To remove free siRNA, the mixture was washed with cold PBS three times by ultracentrifugation at 100,000 × g at 4℃ for 1 h and resuspended in PBS.

Experimental animals and treatment intervention

C57BL/6 mice were purchased from Changzhou Cavens Laboratory Animal Co., LTD. All animal care and experimental procedures are approved by the Experimental Animal Care and Use Ethics Committee of Jiangsu University in accordance with the Chinese Animal Welfare Law (Approval no. UJS-IACUC-AP-2022031502). All animal experiments strictly follow the recommendations of pharmacological studies. All animals underwent a 12-hour light/12-hour dark cycle at 23℃ ± 2℃ and 55% ± 5% relative ambient humidity. After one week of adaptation, the mice were randomly grouped and the mouse models were established.

In recent years, a growing number of studies have used fat-rich diets to model human MASLD, which are collectively referred to as "high-fat diets" (HFD). The HFD diet can mimic the full metabolic and histological features of MASLD in humans, including (but not limited to) obesity, insulin resistance, and most importantly, liver inflammation and fibrosis. To establish a steatosis mouse model, male C57BL/6 mice (male, 6–8 weeks old, 16–20 g) were fed a normal control diet (NCD, 10% dietary fat, $n = 6$) and a high-fat diet (HFD, 60% dietary fat, $n = 18$) for 18 weeks. After 18 weeks, HFD-fed mice were randomly divided into four groups: PBS (HFD + PBS, $n = 6$), RBC-EVs (HFD + RBC-EVs, $n = 6$), RBC-EVs@siNC (HFD + RBC-EVs@siNC, $n = 6$) and RBC-EVs@si*Nup85* (HFD + RBC -EVs@ si*Nup85*, $n = 6$) twice a week for 5 weeks and maintained HFD feeding.

Several currently available animal models are based on diets deficient in certain essential nutrients to induce a liver phenotype similar to that of human MASLD. Among these, methionine-choline deficient (MCD) diets have been widely used in the past to study the occurrence and progression of MASLD. A major advantage of the MCD diet is that it rapidly induces hepatic steatosis and inflammation, followed by significant tissue damage and fibrosis within a few weeks of feeding (usually after 2 to 8 weeks). Therefore, we established another mouse model of steatosis: C57BL/6 mice(male, 6–8 weeks old, 16–20 g) on a normal control diet (NCD, 10% dietary fat, $n = 6$) and a methionine-choline-deficient diet (MCD, $n = 6$) maintained for 8 weeks.

After maintaining a specific diet, the weight of the mice was measured weekly. The mice fasted for 12 h before being euthanized. After the blood of the mice was collected, the livers were removed, weighed and further analyzed.

Fatty acid treatment

We used a fat-overloading model, mixing oleic acid (OA) (Sigma, USA, 07501) and palmitic acid (PA) (Sigma, USA, P9767) in a 2:1 ratio, to establish a lipid accumulation model to induce hepatocytes. This model has been shown to mimic the MASLD characteristics with low level of toxicity to the cells. Briefly, after the cell confluence reached 80%, the HepG2, AML12 and MPH cells were treated with a mixture of 660 μM OA and 330 μM PA with 10% BSA solution (1 mM PAOA) for 12–24 h respectively. Control groups in all experiments were incubated with 10% fatty acid-free BSA without PA and OA.

Protein-protein Docking

The X-ray crystal structures of NUP85 were obtained from the Protein Data Bank. The predicted structures of SLC27A1 were generated using AlphaFold. To ensure the accuracy of the docking results, the protein was prepared with AutoDockTools-1.5.7, during which water molecules were manually removed, and the polar hydrogens were added. Protein-protein docking was conducted using the Docking Web Server (GRAMM). The resulting protein-protein complex was also manually optimized by removing water and adding polar hydrogen by the AutoDockTools-1.5.7. Finally, the protein-protein interactions were predicted and the interaction figure was generated by PyMOL (https://pymol.org).

Cell transfection of plasmid

The *NUP85* overexpression plasmid (pcDNA3.1–3×Flag-C-p*NUP85*) (sequence information is shown in supplementary file 2) and control plasmid (pcDNA3.1–3×Flag-C-pCtr), along with the *SLC27A1* knockdown plasmid (pGPU6-GFP-Neo-sh*SLC27A1*) (Sequence: GCC CTT AAA TGA GGC AGT CTA) and its control plasmid (pGPU6-GFP-Neo-shRNA), were obtained from Hunan Fenghui Biological Co., Ltd. These plasmids were transfected into HepG2 and AML12 cells using Lipofectamine 2000 (Invitrogen, USA, 11668019), following the manufacturer's instructions. Seventy-two hours after transfection, qRT-PCR and western blot were used to verify the expression levels of NUP85 and SLC27A1.

Cell transfection of siRNA

Mus-*Nup85* siRNA, Homo-*NUP85* siRNA, FAM siRNA and control NC siRNA were transfected into HepG2 and AML12 cells using Lipofectamine 2000 (Invitrogen, USA, 11668019) according to the manufacturer's instructions. Seventy-two hours post-transfection, qRT-PCR and western blot analyses were conducted to verify the expression levels of NUP85.

Co-immunoprecipitation (Co-IP)

The primary antibodies used in this experiment were NUP85, SLC27A1 and IgG (Beyotime, Shanghai, China). HepG2 cells were harvested and lysed in immunoprecipitation lysis buffer for 30 min. The cell lysates were incubated overnight at 4℃ with the corresponding antibody (3 μg) or IgG as the negative control. Protein A/G agarose beads (Beyotime, Shanghai, China) were then added and incubated at 4℃ for 4 h. After washing the beads 3 times with lysis buffer, the beads were suspended in 30 μL lysis buffer and boiled with 1 × SDS-PAGE Protein Loading Buffer (Biosharp, China, BL502B), and the protein samples were analyzed by western blot analysis.

Treatment of lipotoxic injured hepatocytes with RBC-EVs

HepG2 and AML12 cells were cultured in 6-well cell culture plates or 24-well cell culture plates. When the cell fusion reached 50–60%, the cells were damaged by adding a concentration of 1 mM PAOA for 24 h. Then, the lipotoxic hepatocytes were treated with RBC-EVs@siNC and RBC-EVs@ si*Nup85* for 24 h, respectively, followed by further experiments.

RBC-EVs internalization assay

Dir dye (UElandy, China, D4006) was used to label RBC-EVs according to the manufacturer's instructions. HepG2 and AML12 cells were incubated with Dir-labeled RBC-EVs for 24 h, and then fixed with 4% paraformaldehyde. The actin cytoskeleton was visualized with anti-β-actin primary antibody and its corresponding fluorescent secondary antibody, and the nucleus was detected with Hoechst 33,342 dye (Beyotime, China, C1025). Fluorescence microscopy (Olympus, Tokyo, Japan) was employed to evaluate the internalization of RBC-EVs.

Cell treatment with GW9662 and Darglitazone

Preparation of GW9662 (PPAR-γ signaling pathway inhibitor) reserve solution: Dissolve 1 mg of GW9662 sample (MCE, USA, HY-16578) in 3.6 mL DMSO solution (Sigma-Aldrich, USA, 472301) at a concentration of 1 mM; Preparation of darglitazone (PPAR-γ signaling pathway agonist) reserve solution: Dissolve 1 mg of darglitazone sample (Glpbio, China, GC11477) in 2.4 mL DMSO solution at a concentration of 1 mM. HepG2 cells were cultured in 6-well cell plates or 24-well cell plates. When the cell confluence reached 50–60%, different concentrations of GW9662 (1 μM and 5 μM) were added, respectively, and the cells were treated for 24 h, and subsequent experiments were conducted. Similarly, the cells were treated with different concentrations of Darglitazone (5 μM and 10 μM) for 24 h and subsequent experiments were carried out. DMSO-treated cells (0.1%) were used as solvent controls.

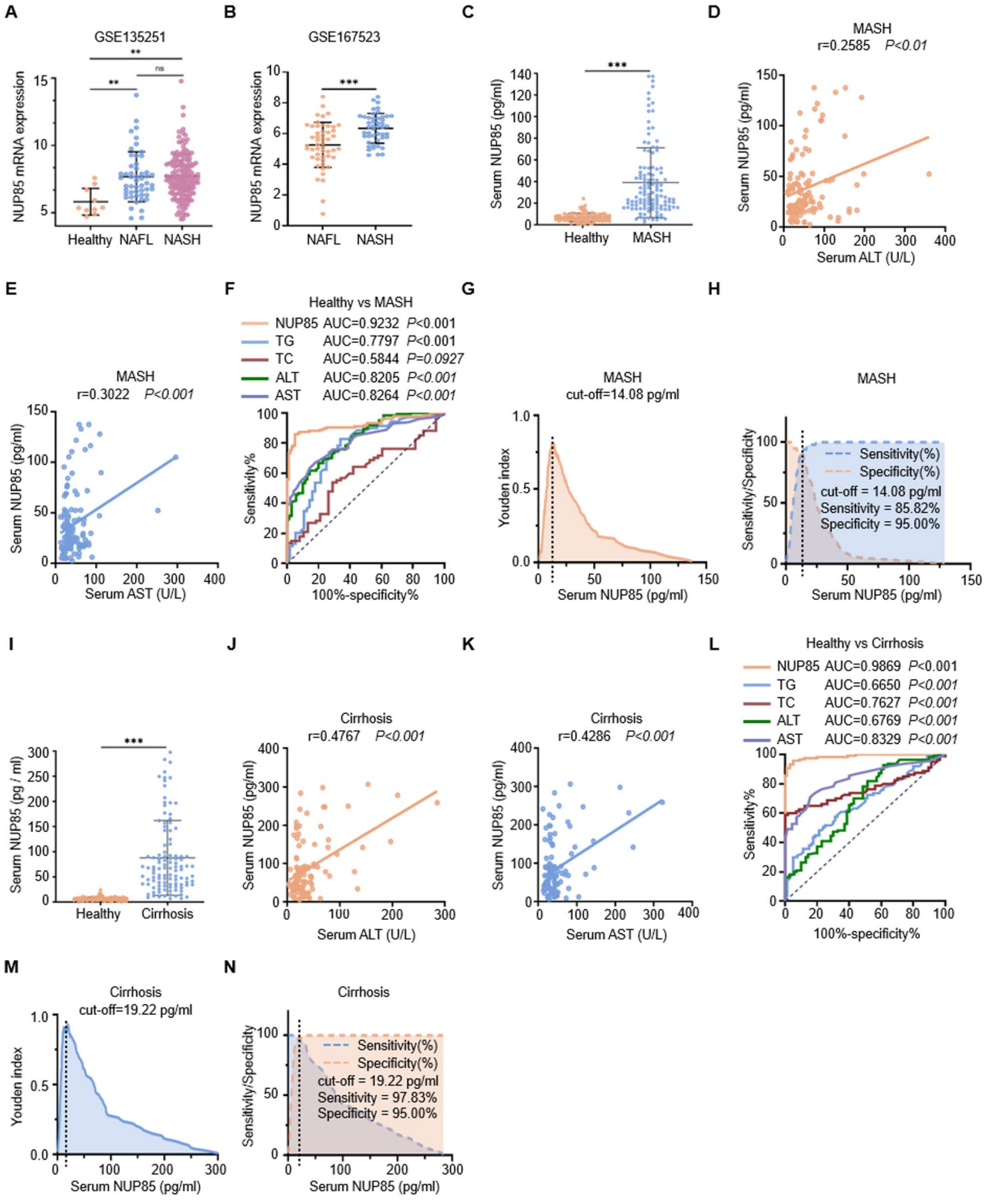


Fig. 1 (See legend on next page.)

(See figure on previous page.)

Fig. 1 Predictive Value of Serum NUP85 Content in Patients with MASH and Cirrhosis **A**. The expression of NUP85 in liver tissue of MASLD patients was analyzed using data from a public database. **B**. The expression of NUP85 in liver tissue of MASLD patients was further examined using data from another public database (GSE167523). **C**. ELISA kits were employed to measure serum NUP85 levels in both healthy individuals ($n = 100$) and MASH patient ($n = 120$). **D**. The correlation between serum NUP85 and ALT levels in MASH patients was evaluated. **E**. The correlation between serum NUP85 and AST levels in MASH patients was assessed. **F**. A receiver operating characteristic (ROC) curve was generated for serum NUP85, ALT, AST, TG, and TC levels in a cohort of 120 diagnosed MASH patients and 100 normal subjects, with the area under the curve (AUC) indicated in the figure. **G**. The Youden index for serum NUP85 in NASH patients was calculated. **H**. Diagnostic sensitivity and specificity curves for serum NUP85 in patients with MASH were established. I. ELISA kits were also utilized to detect serum NUP85 levels in healthy individuals ($n = 100$) and patients with liver cirrhosis ($n = 110$). **J**. The correlation between serum NUP85 and ALT levels in NASH patients was analyzed. **K**. The correlation between serum NUP85 and AST levels in NASH patients was similarly explored. **L**. An ROC curve was constructed for serum NUP85, ALT, AST, TG, and TC levels in a group of 110 patients diagnosed with cirrhosis and 100 normal subjects, with the AUC presented in the figure. **M**. The Youden index for serum NUP85 in cirrhosis patients was determined. **N**. Finally, diagnostic sensitivity and specificity curves for serum NUP85 in patients with cirrhosis were generated. All data are expressed as the mean ± SD. ns: no significance; * $P < 0.05$; ** $P < 0.01$; *** $P < 0.001$

Mouse primary hepatocyte extraction

Six-week old C57BL/6 male mice were anaesthetised by intraperitoneal injection of 0.3% sodium pentobarbital (50 mg/kg, P-010, Merck, germany). The liver was perfused from the inferior vena cava with a pre-heated (37℃) calcium-free solution (containing 8.3 g NaCl, 0.5 g KCl, 2.4 g HEPES, and 0.015 g EDTA per liter of solution) until the liver was devoid of blood. Subsequently, a solution of type IV collagenase (Sigma, USA, C5138) heated to 37℃ was perfused into the liver. The perfusion was stopped when the liver collapsed and cracks appeared on its surface. The liver was then quickly excised and in cold DMEM/F12 medium containing 10% fetal bovine serum to release the isolated hepatocytes. The obtained cell suspension, after being centrifuged at 40 g for 1 min, was re-suspended in cold DMEM/F12, and the cell pellet was filtered through a 100 μm cell strainer, and the precipitate was collected by centrifugation. The pellet was re-suspended in a mixture of 5 mL DMEM/F12, 4.5 mL Percoll (Sigma, USA, P4937), and 0.5 mL 10× phosphate-buffered saline(Beyotime, China, ST476), and centrifuged at 80 g for 10 min to obtain purified MPHs. Resuspend the precipitate with DMEM/F12 medium, and seeded in 6-well or 24-well plates at a density of 5×10^5 cells/well.

siRNA efficiency of loading to RBC-EV

The fluorescence intensity of free siRNA-FAM, siRNA-FAM after electroporation into RBC-EV, and after sonication cleavage of RBC-EV@siRNA-FAM were detected, respectively. The relative fluorescence intensities of the three groups were then compared.

Serum stability assay

To confirm the serum stability of the siRNA delivery system, free *Nup85* siRNA or RBC-EV@si*Nup85* were incubated with 5% FBS. Aliquots of different incubation times from each group were subject to electrophoresis on an agarose gel and then observed on a UV illuminator.

Statistical analysis

All experiments (including cell and mouse-based experiments) included biological replicates and were repeated at least three times. The data represent the mean ± SD. The Pearson normality test and D'Agostino was used to determine the normal distribution. Prism software (GraphPad 8.0, San Diego, CA) was used for statistical analysis. A one-way ANOVA, two-way ANOVA or t-test was utilized to assess significant differences between groups. All statistical tests were two-tailed, $P < 0.05$ was defined as significant, and report the 95% confidence interval.

Results

Predictive value of serum NUP85 content in patients with MASH and cirrhosis

We first confirmed the association between elevated liver *NUP85* mRNA levels and the progression of MASLD by analyzing published transcriptome profiles from two independent MASLD patient cohorts (GSE135251 and GSE167523) (Fig. 1A-B). Subsequently, we collected serum samples from healthy individuals ($n = 100$) and MASH patients ($n = 120$), utilizing an ELISA kit to measure NUP85 levels in the serum. Compared to serum from healthy individuals, NUP85 protein levels were significantly elevated in the serum of MASH patients, showing a positive correlation with alanine aminotransferase (ALT) ($r = 0.2585$, $P < 0.01$) and aspartate aminotransferase (AST) ($r = 0.3022$, $P < 0.001$) levels (Fig. 1C-E). The area under the curve (AUC) analysis indicated that the diagnostic efficiency of serum NUP85 for MASH was 0.9232, outperforming traditional serum markers such as ALT, AST, triglycerides (TG) and total cholesterol (TC) (Fig. 1F). The diagnostic threshold for serum NUP85 in NASH was determined to be 14.08 pg/ml, with high sensitivity (85.82%) and specificity (95.00%) (Fig. 1G-H). Furthermore, NUP85 protein levels were significantly higher in the serum of cirrhosis patients ($n = 110$) compared to healthy individuals ($n = 100$), and were positively correlated with ALT ($r = 0.4767$, $P < 0.001$) and AST ($r = 0.4286$, $P < 0.001$) levels (Fig. 1I-K). AUC analysis revealed that the diagnostic efficiency of serum NUP85 for liver cirrhosis was 0.9869, again surpassing traditional serum markers ALT, AST, TG, and TC (Fig. 1L). The diagnostic threshold for serum NUP85 in liver cirrhosis

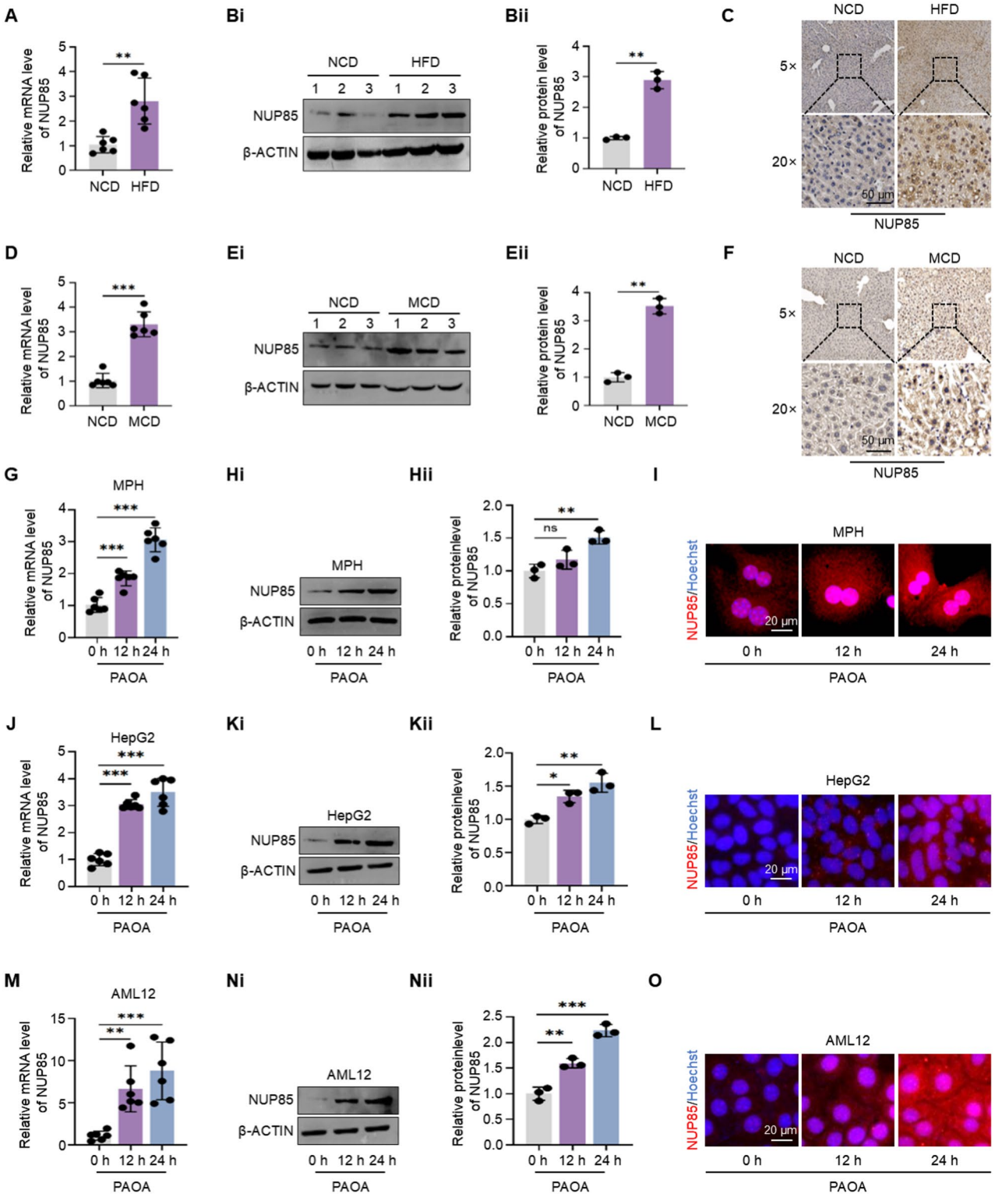


Fig. 2 (See legend on next page.)

was established at 19.22 pg/ml, exhibiting high sensitivity (97.83%) and specificity (95.00%) (Fig. 1M-N). Compared with healthy individuals, the serum NUP85 protein levels in patients with liver cirrhosis due to other causes ($n = 30$) (including hepatitis B-related cirrhosis, hepatitis C-related cirrhosis, alcoholic cirrhosis, primary biliary cirrhosis and autoimmune hepatitis-related cirrhosis) were also significantly elevated (Fig. S10A). These

(See figure on previous page.)

Fig. 2 The expression level of NUP85 is elevated in the liver of model mice and lipotoxic hepatocytes. **(A)** Relative levels of *Nup85* mRNA in the livers of mice fed normal chow versus high-fat chow ($n=6$). **(B)** Western blot reveals NUP85 protein expression in the livers of mice on a normal diet compared to those on a high-fat diet, including statistical results ($n=3$). **(C)** Representative immunohistochemical staining images illustrating NUP85 expression in the livers of mice fed normal chow and high-fat chow. Scale bar, 50 μm. **(D)** Relative levels of *Nup85* mRNA in the livers of mice fed normal chow and MCD chow ($n=6$). **(E)** Western blot detects NUP85 protein expression in the livers of mice on a normal diet versus those on an MCD diet, along with statistical results ($n=3$). **(F)** Representative immunohistochemical staining images showing NUP85 expression in the livers of mice fed normal chow and MCD chow. Scale bar, 50 μm. **G**, **J**, **M.** qRT-PCR analysis measured the relative levels of *Nup85* mRNA in MPH, HepG2, and AML12 cells after treatment with 1 mM PAOA for 0, 12, and 24 h, respectively ($n=6$). **H**, **K**, **N.** Western blot assessed NUP85 protein expression and statistical results in MPH, HepG2, and AML12 cells treated with 1 mM PAOA for 0, 12, and 24 h, respectively ($n=3$). **I**, **L**, **O.** Immunofluorescence staining of NUP85 in MPH, HepG2, and AML12 cells after treatment with 1 mM PAOA for 0, 12, and 24 h, respectively. Scale bar, 20 μm. All data are expressed as the mean ± SD. ns: no significance; * $P<0.05$; ** $P<0.01$; *** $P<0.001$

findings indicate that serum NUP85 content holds significant value in diagnosing patients with MASH and cirrhosis.

The expression level of NUP85 is elevated in the liver of model mice and lipotoxic hepatocytes

Histological examination using hematoxylin-eosin (HE) staining (Fig. S1A-B) and Oil Red O staining (Fig. S1C) revealed that, compared to normal control diet (NCD) mice, vacuolar degeneration and fat deposition in the hepatocytes of high-fat diet (HFD) and methionine-choline deficient diet (MCD) mice were significantly more pronounced. Furthermore, the expression of NUP85 mRNA and protein in the liver tissue of HFD mice was significantly elevated when compared to NCD mice (Fig. 2A-B). Immunohistochemical analysis further confirmed an increase in NUP85 protein expression (Fig. 2C). Similarly, both NUP85 mRNA and protein levels were significantly higher in the liver tissue of MCD mice compared to NCD mice (Fig. 2D-E), with immunohistochemistry results corroborating a notable increase in NUP85 levels (Fig. 2F).

MASLD is characterized by excessive lipid deposition in hepatocytes. In this study, we investigated the effect of hepatocyte lipid deposition on NUP85 expression. PAOA was observed to induce lipid deposition in MPH (Fig. S1D), HepG2 (Fig. S1E), and AML12 (Fig. S1F) cells. Notably, as the duration of induction increased, lipid deposition was significantly exacerbated, accompanied by marked increases in the mRNA, protein, and fluorescence levels of NUP85 (Fig. 2G-O).

Additionally, compared to healthy individuals, liver tissue from MASH patients exhibited significant vacuolar degeneration, while cirrhosis patients displayed notable fibrosis (Fig. S2A). In comparison to healthy individuals, the expression of NUP85 protein in the liver tissues of patients with MASH and cirrhosis was significantly elevated and correlated with disease severity (Fig. S2B).These findings suggest that NUP85 expression is increased in the liver tissues of HFD and MCD model mice, as well as in PAOA-induced hepatocytes.

NUP85 aggravates PAOA-induced hepatocyte lipid deposition, oxidative stress, and inflammatory response

We further investigated the effects of NUP85 knockdown and overexpression on lipid metabolism in hepatocytes. NUP85 siRNA was designed and transfected into HepG2 cells. The levels of NUP85 mRNA (Fig. 3A), NUP85 protein (Fig. 3B), and fluorescence (Fig. 3C) were significantly reduced, confirming the successful inhibition of NUP85 expression. Under PAOA treatment, HepG2 cells transfected with NUP85 siRNA showed significantly enhanced viability compared to the siRNA control group (Fig. S9A). Furthermore, we observed that NUP85 knockdown significantly decreased PAOA-induced lipid deposition in hepatocytes (Fig. 3D), as well as intracellular triglyceride (TG) levels (Fig. 3E) and free fatty acid (FFA) levels (Fig. 3F). The knockdown of *NUP85* also regulates the expression levels of oxidative stress-related indicators: Compared to the control group, the knockdown of *NUP85* resulted in decreased levels of malondialdehyde (MDA) (Fig. 3G), increased enzyme activity of superoxide dismutase (SOD) (Fig. 3H), elevated levels of glutathione (GSH) (Fig. 3I), and reduced levels of reactive oxygen species (ROS) (Fig. 3J). In addition, compared to the NC-siRNA/PAOA group, the mRNA expression levels of several genes in the *NUP85*-siRNA/PAOA group were altered, highlighting their crucial role in the progression of MASLD. Among the lipogenesis-related genes (Fig. 3K), the expression levels of sterol regulatory element-binding protein 1 (*SREBP1*), acetyl CoA carboxylase (*ACC1*) and fatty acid synthase gene (*FASN*) decreased. Regarding inflammation-related genes (Fig. 3L): the expression levels of tumor necrosis factor α (*TNF*), interleukin-1 β (*IL1B)* and interleukin-6 (*IL6)* decreased. For β-oxidation-related genes (Fig. 3M): the expression levels of peroxisome proliferator-activated receptor (*PPARA*), carnitine palmitoyltransferase 2 (*CPT2*), and long-chain acyl-CoA dehydrogenase (*LCAD*) increased. Lastly, concerning fatty acid uptake genes (Fig. 3N): the expression levels of fatty acid transport protein 1 (*FATP1*), fatty acid transport protein 4 (*FATP4*), and cluster of differentiation 36 (*CD36*) decreased. In summary, these results indicate that *NUP85* knockdown

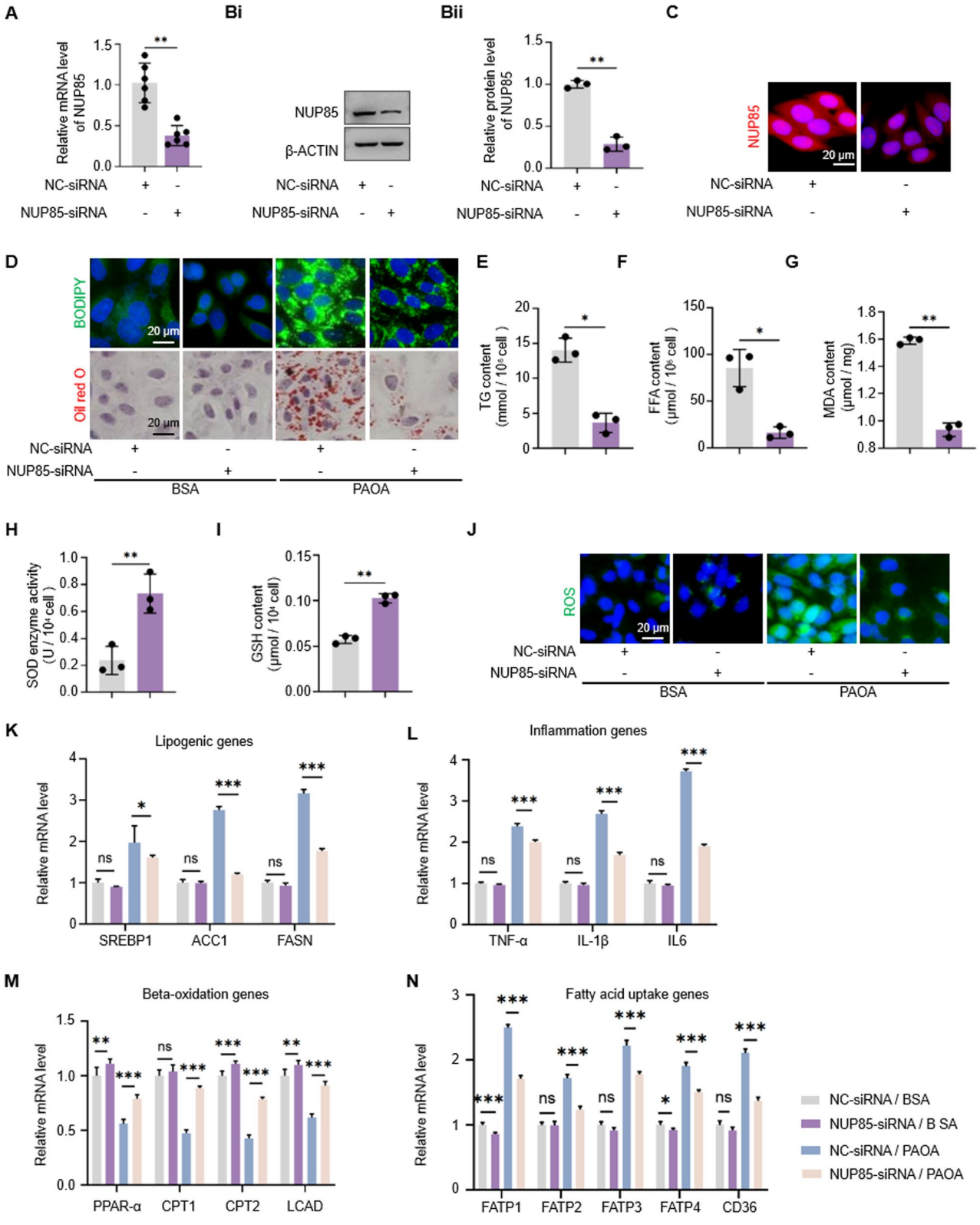


Fig. 3 (See legend on next page.)

(See figure on previous page.)

Fig. 3 Ablation of NUP85 alleviates PAOA-induced hepatocyte lipid deposition, oxidative stress, and inflammatory response. **A**. qRT-PCR was utilized to assess the expression level of *NUP85* following the transfection of control siRNA and *NUP85*-siRNA ($n=6$). **B**. Western blot was performed to determine the expression level of NUP85 post-transfection with control siRNA and *NUP85*-siRNA ($n=3$). **C**. Cell immunofluorescence analysis was conducted to evaluate the expression level of NUP85 after transfection with control siRNA and *NUP85*-siRNA. Scale bar, 20 μm. **D**. BODIPY and Oil Red O staining were employed to visualize intracellular lipid droplets following transfection with control siRNA and *NUP85*-siRNA, along with induction by 1 mM PAOA. Scale bar, 20 μm. **E**-**J**. HepG2 cells were transfected with either control siRNA or *NUP85*-siRNA, and subsequently induced with 1 mM PAOA to measure levels of intracellular TG (E), FFA (F), lipid oxidation as measured by MDA content (G), SOD enzyme activity (H), GSH content (I), and ROS (J) ($n=3$).Scale bar, 20 μm. **K**-**N**. The detection of transfected *NUP85*-siRNA, induced by 1 mM PAOA, was associated with lipogenic (K), inflammation (L), β-oxidation (M) and fatty acid uptake (N), focusing on the expression of relevant genes in HepG2 cells ($n=6$). All data are expressed as the mean ± SD. ns: no significance; * $P<0.05$; ** $P<0.01$; *** $P<0.001$

can alleviate PAOA-induced lipid deposition, oxidative stress, and inflammatory responses in hepatocytes.

Similarly, we constructed the *NUP85* overexpression plasmid, pcDNA3.1–3×Flag-*NUP85*, and transfected it into HepG2 cells. The levels of NUP85 mRNA (Fig. 4A), protein (Fig. 4B) and fluorescence (Fig. 4C) were significantly increased. Under PAOA treatment, HepG2 cells overexpressing NUP85 exhibited a significant decrease in cell viability compared to the empty vector group (Fig. S9B). Our study confirmed that PAOA-induced hepatocyte lipid deposition (Fig. 4D), as well as intracellular TG (Fig. 4E) and FFA levels, were significantly elevated following *NUP85* overexpression (Fig. 4F). Indicators associated with oxidative stress, including increased MDA levels (Fig. 4G), decreased SOD enzyme activity (Fig. 4H), decreased GSH levels (Fig. 4I), and ROS levels (Fig. 4J) were significantly increased. The expression levels of lipogenesis-related genes (Fig. 4K), including sterol regulatory element-binding protein 1 (*SREBP1*) and acetyl-CoA carboxylase 1 (*ACC1*) were upregulated. The expression of inflammation-related genes (Fig. 4L), such as tumor necrosis factor (*TNF*), interleukin-1 β (*IL1B)* and interleukin-6 (*IL6*) was increased. The gene expression of β-oxidation-related genes (Fig. 4M), namely peroxisome proliferator-activated receptor (*PPARA*) and long-chain acyl-CoA dehydrogenase (*LCAD*), was downregulated. The expression levels of fatty acid uptake genes (Fig. 4N), including fatty acid transport protein 1 (*FATP1*), fatty acid transport protein 4 (*FATP4*), and cluster of differentiation 36 (*CD36*), were increased. In summary, these results indicate that overexpression of *NUP85* exacerbates PAOA-induced lipid deposition, oxidative stress, and inflammatory response in hepatocytes. Therefore, we conclude that NUP85 plays a significant role in aggravating lipid deposition, oxidative stress, and inflammatory responses in lipotoxic hepatocytes.

NUP85 promotes MASLD by regulating SLC27A1

To further investigate the molecular mechanism by which NUP85 regulates lipid metabolism, we utilized the STRING database (https://string-db.org/) to constr uct a protein-protein interaction (PPI) network. To further investigate the molecular mechanisms by which NUP85 regulates lipid metabolism, we utilized the STRING database (https://string-db.org/) to construct a protein-protein interaction (PPI) network. Our analysis revealed that NUP85 interacts with SLC27A1 (Fig. 5A). Subsequently, we predicted the interaction sites between NUP85 and SLC27A1 through molecular docking experiments (Fig. 5B). Co-immunoprecipitation (Co-IP) results (Fig. 5C-D) confirmed the binding of NUP85 to SLC27A1 in HepG2 cells. In HepG2 cells overexpressing Flag-NUP85, SLC27A1 was also shown to bind to Flag-NUP85 (Fig. 5E). Immunofluorescence staining of mouse liver tissues demonstrated the interaction between SLC27A1 and NUP85 proteins (Fig. 5F). Additionally, cellular immunofluorescence staining results (Fig. 5G-H) further confirmed the binding of NUP85 to SLC27A1. Furthermore, results from qRT-PCR (Fig. S3A), Western blot (Fig. S3B), and cellular immunofluorescence (Fig. S3C) indicated that PAOA induced the expression of SLC27A1 in HepG2 cells. Knockdown of SLC27A1 (Fig. S3D-E) attenuated PAOA-induced intracellular lipid deposition (Fig. S3F) and decreased levels of intracellular TG (Fig. S3G) and FFA (Fig. S3H).

In addition, the results from qRT-PCR (Fig. 5I-J) and western blot (Fig. 5K-L) demonstrated that the inhibition of NUP85 led to a down-regulation of SLC27A1 expression levels in PAOA-induced HepG2 cells, while the overexpression of NUP85 resulted in an up-regulation of SLC27A1. In conclusion, NUP85 appears to interact with SLC27A1 in HepG2 cells, playing a regulatory role. To further confirm that NUP85 acts through SLC27A1, we co-transfected PAOA-induced HepG2 cells with pcDNA3.1–3×Flag-*NUP85* and *SLC27A1*-shRNA. The results from qRT-PCR (Fig. 5M) and western blot (Fig. 5N) confirmed the success of the transfection. Following the knockdown of *SLC27A1*, the effects of NUP85 on promoting cellular lipid deposition were alleviated (Fig. 5O), and the levels of triglycerides (TG) (Fig. 5P) and free fatty acids (FFA) (Fig. 5Q) were reduced. Thus, NUP85 may promote the development of MASLD by regulating SLC27A1.

NUP85 regulates lipid deposition and inflammatory response through the PPAR-γ signaling pathway

It has been demonstrated that the knockdown of SLC27A1 leads to a reduction in PPAR-γ expression [23].

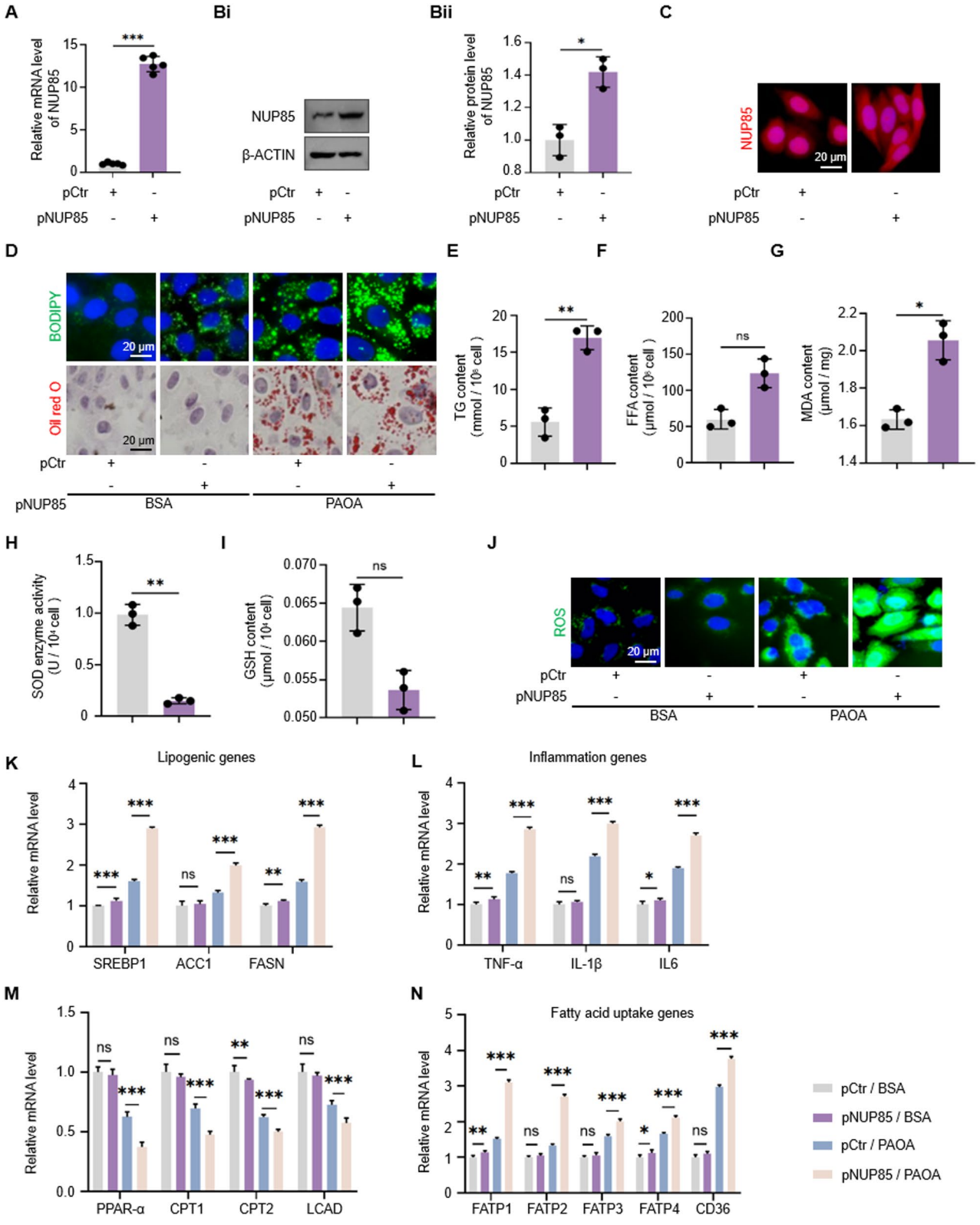


Fig. 4 (See legend on next page.)

(See figure on previous page.)

Fig. 4 NUP85 overexpression aggravates PAOA-induced hepatocyte lipid deposition, oxidative stress, and inflammatory response. **A**. qRT-PCR was utilized to assess the expression level of *NUP85* following transfection with pcDNA3.1−3×Flag-*NUP85* ($n=5$). **B**. Western blot was performed to evaluate the expression level of NUP85 after transfection with the control vector (pCtr) and pcDNA3.1−3×Flag-NUP85 ($n=3$). **C**. Cell immunofluorescence was employed to detect the expression level of NUP85 after transfection with pcDNA3.1−3×Flag-NUP85. Scale bar, 20 μm. **D**. BODIPY and Oil Red O staining were used to detect lipid levels following transfection with pcDNA3.1−3×Flag-*NUP85* and induction with 1 mM PAOA. Scale bar, 20 μm. **E**-**J**. HepG2 cells were transfected with either the control vector (pCtr) or pcDNA3.1−3×Flag-*NUP85*, and subsequently induced with 1 mM PAOA to measure intracellular TG levels (E), FFA (F), lipid oxidation as measured by MDA content (G), SOD enzyme activity (H), GSH content (**I**), and ROS levels (**J**) ($n=3$). Scale bar, 20 μm. K-N. The association between transfection of pcDNA3.1−3×Flag-*NUP85* and various biological processes, including lipogenic (K), inflammation (L), β-oxidation (M) and fatty acid uptake (N), was assessed by measuring the expression of related genes in HepG2 cells ($n=6$). All data are expressed as the mean ± SD. ns: no significance; * $P<0.05$; ** $P<0.01$; *** $P<0.001$

Enhanced expression of PPAR-γ and lipogenic genes is observed in animal models and in the fatty livers of patients with non-alcoholic fatty liver disease (NAFLD) [24]. Initially, western blot analysis revealed reduced levels of PPAR-γ protein following SLC27A1 knockdown (Fig. S4A). Similarly, the knockdown of NUP85 resulted in decreased PPAR-γ protein levels (Fig. 6A), while overexpression of NUP85 led to increased PPAR-γ protein levels (Fig. 6B). Notably, both NUP85 and SLC27A1 can simultaneously regulate PPAR-γ expression; compared to the control plasmid-transfected group, PPAR-γ protein expression increased after NUP85 overexpression and decreased following SLC27A1 knockdown. When NUP85 was overexpressed while SLC27A1 was knocked down, the PPAR-γ protein expression level was intermediate between the two conditions (Fig. 6C). Subsequently, we treated the cells with the PPAR-γ inhibitor GW9662 and the agonist Darglitazone, which inhibited (Fig. S4B) and promoted (Fig. S4C) PPAR-γ protein expression, respectively. Inhibition of the PPAR-γ signaling pathway using GW9662 attenuated cellular lipid deposition (Fig. S4D), whereas activation of this pathway with Darglitazone exacerbated cellular lipid deposition (Fig. S4E). Compared to the control group, overexpression of NUP85 significantly increased PPAR-γ protein expression, exacerbating cellular lipid deposition and inflammatory responses. Conversely, treatment with the inhibitor GW9662 reduced PPAR-γ protein expression and mitigated both cellular lipid deposition and inflammatory responses. Notably, the simultaneous overexpression of NUP85 alongside GW9662 treatment resulted in intermediate levels of PPAR-γ protein expression, cellular lipid deposition, and inflammation (Fig. 6D, F, H). In contrast, knockdown of NUP85 led to decreased PPAR-γ protein expression and a reduction in cellular lipid deposition and inflammatory responses compared to the control group. Treatment with the agonist Darglitazone, however, increased PPAR-γ protein expression along with cellular lipid deposition and inflammatory responses. Furthermore, knockdown of NUP85 combined with Darglitazone treatment yielded intermediate levels of PPAR-γ protein expression, cellular lipid deposition, and inflammation (Fig. 6E, G, I). These findings suggest that NUP85 modulates lipid deposition and inflammation via the PPAR-γ signaling pathway.

RBC-EVs@siNUP85 inhibits PAOA-induced hepatocyte steatosis and inflammation

The delivery of siRNA represents a promising strategy for the treatment of Metabolic Dysfunction-associated Steatotic Liver Disease (MASLD), with red blood cell-derived extracellular vesicles (RBC-EVs) offering an efficient and non-immunogenic delivery option. In this study, we investigated the therapeutic potential of RBC-EVs loaded with *Nup85* siRNA (RBC-EVs@si*Nup85*) in the repair of liver injury in mice subjected to a high-fat diet (HFD). Initial in vitro experiments utilized red blood cells extracted from healthy O-type blood donors. The RBC-EVs were isolated by processing through a polycarbonate membrane filter, and NUP85 siRNA was introduced into the RBC-EVs via electroporation, resulting in the formation of RBC-EVs@si*Nup85*, which was then co-cultured with target cells (Fig. 7A). Western blot analysis demonstrated that RBC-EVs express common extracellular vesicle markers such as ALIX and TSG101, as well as the RBC marker hemoglobin subunit alpha (HBA), while lacking expression of the endoplasmic reticulum protein Calnexin (Fig. 7B). The isolated RBC-EVs exhibited an average particle size of approximately 100 nm (Fig. 7C-D).

Stability tests demonstrated that free *Nup85* siRNA degraded within 24 h in 50% FBS, whereas *Nup85* siRNA encapsulated in RBC-EVs remained stable (Fig. 7E). The siRNA loading efficiency experiments revealed that FAM-labeled siRNA could be effectively introduced into RBC-EVs via electroporation (Fig. 7F). RBC-EVs@si*Nup85*, labeled with Dir, were co-cultured with AML12 or HepG2 cells, and the results indicated that RBC-EVs could be internalized by the cells, with a distribution observed around the nucleus (Fig. S5A, D). Both Dir-labeled RBC-EVs and FAM-labeled siRNA were localized within the cells (Fig. S5B, E). Subsequently, we evaluated the effects of RBC-EVs@siNUP85 and RBC-EVs@siNC on the proliferation of PAOA-treated AML12 and HepG2 cells using the CCK-8 kit. Compared to the PBS control group, cell proliferation was significantly enhanced after incubation with RBC-EVs@siNUP85 (Fig. S5C,

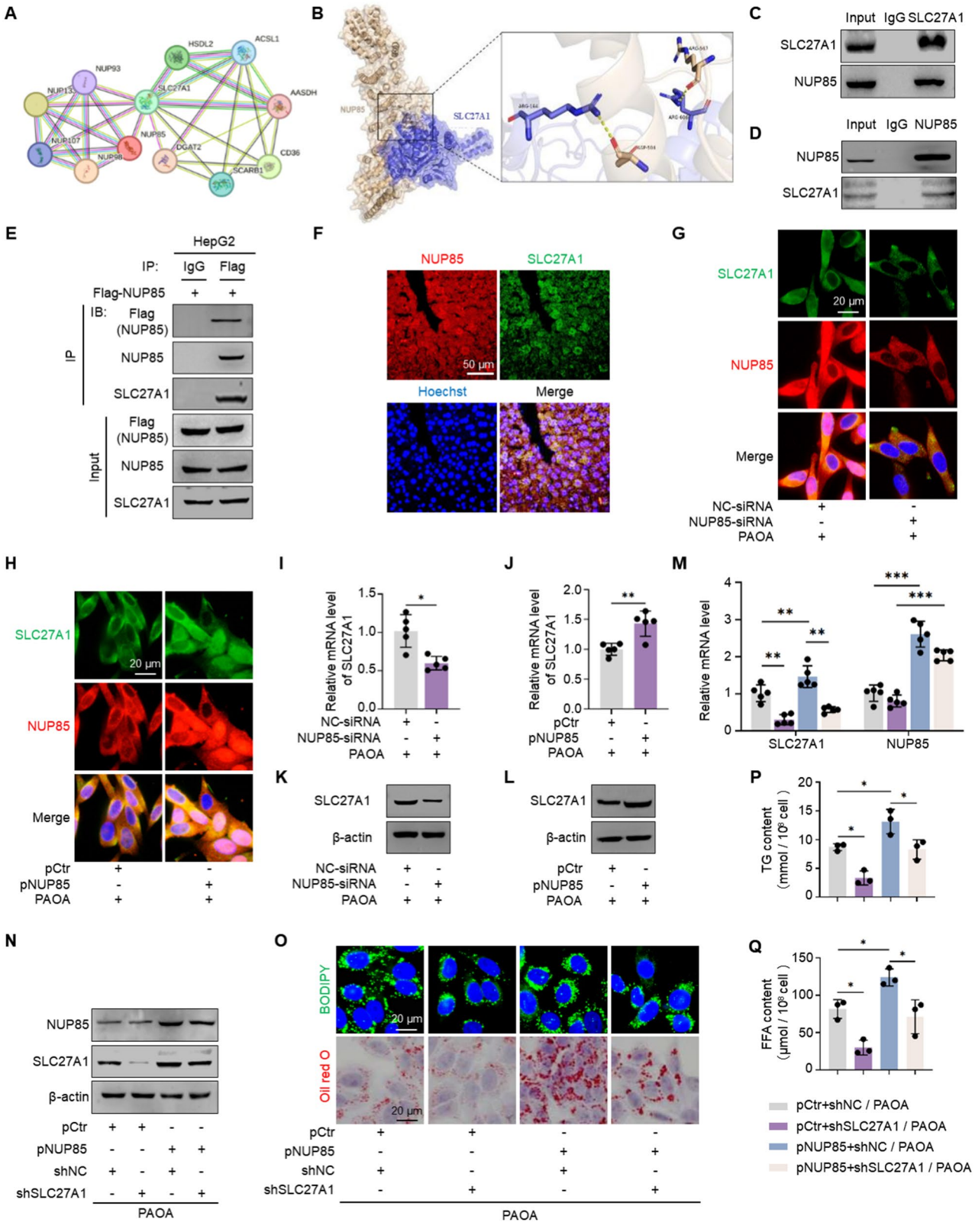


Fig. 5 (See legend on next page.)

(See figure on previous page.)

Fig. 5 NUP85 promotes MASLD by regulating SLC27A1. **(A)** The STRING database was utilized to construct a protein-protein interaction (PPI) network aimed at analyzing and identifying the interaction between NUP85 and SLC27A1. **(B)** A schematic diagram illustrating the three-dimensional structure of the interaction model between NUP85 and SLC27A1 is presented. **C-D.** Co-immunoprecipitation (Co-IP) results indicate that NUP85 binds to SLC27A1. **E.** Interaction between NUP85 and SLC27A1 by Co-IP in HepG2 cells transfected with Flag-*NUP85*. **F.** Interaction between NUP85 and SLC27A1 in mouse liver tissues. Scale bar, 50 μm. **G-H.** The results for NUP85 (red) and SLC27A1 (green) in cells transfected with either NUP85-siRNA or pcDNA3.1−3×Flag-*NUP85* are shown. **I-L.** The results for *NUP85* and *SLC27A1* mRNA (I-J) and protein (K-L) in cells transfected with either NUP85-siRNA or pcDNA3.1−3×Flag-NUP85 are shown. **M-N.** The mRNA (M) and protein (N) expression levels of NUP85 and SLC27A1 were assessed following simultaneous transfection with SLC27A1-shRNA and pcDNA3.1−3×Flag-NUP85 ($n = 5$). **O.** BODIPY and Oil Red O staining were employed to detect intracellular lipid droplets in HepG2 cells that were simultaneously transfected with pcDNA3.1−3×Flag-*NUP85* and *SLC27A1*-shRNA, and induced with 1 mM PAOA. Scale bar, 20 μm. **P-Q.** Triglyceride and free fatty acid detection kits were utilized to analyze HepG2 cells transfected with pcDNA3.1−3×Flag-*NUP85* and *SLC27A1*-shRNA after induction with 1 mM PAOA, measuring TG (P) and FFA (Q) levels ($n = 3$). All data are expressed as the mean ± SD. ns: no significance; * $P < 0.05$; ** $P < 0.01$; *** $P < 0.001$

F). Treatment with RBC-EVs@siNUP85 significantly inhibited the expression of NUP85 mRNA (Fig. 7G-H) and protein (Fig. 7I-J) in the cells, while also reducing PAOA-induced intracellular lipid deposition (Fig. 7K-L), ROS levels (Fig. 7M-N), and the expression of inflammatory factors (Fig. 7O-P). These findings confirm that RBC-EVs@si*Nup85* effectively inhibits lipid deposition and alleviates inflammatory responses in lipotoxic hepatocytes.

RBC-EVs@si*Nup85* reduces liver injury in HFD-fed mice

Following the administration of RBC-EVs@si*Nup85* via tail vein injection in mice. Histological evaluation through H&E staining revealed no apparent pathological abnormalities in the heart, liver, spleen, lung, or kidney of mice treated with RBC-EV, RBC-EV@siNC, and RBC-EV@siNup85, indicating excellent biosafety (Fig. S6). In vivo imaging demonstrated that Dir-labeled RBC-EVs@si*Nup85* predominantly accumulated in liver tissue 24 h post-injection (Fig. 8A). Immunofluorescence staining of mouse liver tissues indicated that NUP85 was predominantly expressed in hepatocytes (Fig. S8A), with FAM-labelled siRNA and Dir-labelled RBC-EV colocalizing within liver cells (Fig. S8B), and Dir-labelled RBC-EV primarily localized in hepatocytes (Fig. S8C). NUP85 expression was elevated in mice in the high-fat diet (HFD) group compared to those in the normal chow diet (NCD) group. Furthermore, NUP85 expression was significantly reduced in the liver tissues of HFD mice injected with RBC-EVs@si*Nup85* compared to those injected with PBS (Fig. 8B-C, I, Fig. S7A). The liver's appearance transitioned from rough and obscure to smooth and shiny (Fig. 8D), and the mice exhibited weight loss (Fig. 8E). In contrast, food intake did not significantly differ among the various groups, and this trend was consistent throughout the entire treatment period (Fig. S11). Additionally, liver weight was reduced (Fig. 8F), while lipid droplets in liver tissue were significantly diminished (Fig. 8G). Both vacuolar degeneration and ballooning degeneration were notably reduced (Fig. 8H). Moreover, serum levels of ALT (Fig. 8J), AST (Fig. 8K), FFA (Fig. 8L), and TG (Fig. 8M) significantly decreased in mice. Compared to mice injected with PBS, RBC-EV, and RBC-EV@siNC, HFD mice injected with RBC-EVs@si*Nup85* exhibited significantly reduced levels of TG (Fig. 8N), TC (Fig. 8O), FFA (Fig. 8P), and LDL-C (Fig. 8Q) in liver tissue. Compared with the mice injected with PBS, RBC-EV and RBC-EV@siNC, the expressions of inflammatory factors IL6 (Fig. S12A) and TNF-α (Fig. S12B) in the liver tissue were significantly decreased, and the mRNA expressions of IL-1β, IL6 and TNF-α in mice injected with RBC-EVs@siNup85 were significantly reduced (Fig. S12C-E). Compared with the mice injected with PBS, RBC-EV and RBC-EV@siNC, the mRNA expressions of COL1A1, COL3A1, α-SMA and TGF-β were significantly reduced (Fig. S12F-I); as well as the liver tissue collagen deposition (Fig. S12J) and the expression of α-SMA protein (Fig. S12K) in the MASLD mice injected with RBC-EVs@siNup85 were significantly reduced. Compared to the RBC-EV group and the RBC-EV@siNC group, the RBC-EV@siNup85 group of mice revealed no significant differences in body weight, liver weight, serum ALT, AST, FFA, or TG. Collectively, these findings suggest that the targeted delivery of RBC-EVs@si*Nup85* effectively inhibits NUP85 expression in mouse liver tissue, mitigates hepatocyte steatosis, alleviate liver inflammation and fibrosis in mice, and promotes liver injury repair.

Discussion

Early detection and accurate staging of MASLD are crucial for preventing disease progression and its associated complications [25]. Current research is focused on identifying non-invasive markers for MASLD. Our study demonstrates that NUP85 exhibits high sensitivity and specificity for diagnosing MASLD, potentially serving as a novel marker for early detection. Identifying new targets to inhibit steatosis and inflammatory responses is essential for mitigating the progression of MASLD. This study elucidates the role and mechanism of NUP85 in enhancing hepatic lipid metabolism. NUP85 interacts with the fatty acid transporter SLC27A1, thereby activating the PPAR-γ signaling pathway and promoting lipid accumulation in the liver. Importantly, our findings confirm that RBC-EVs carrying siNUP85 effectively inhibit NUP85 expression in mouse livers, reduce lipid

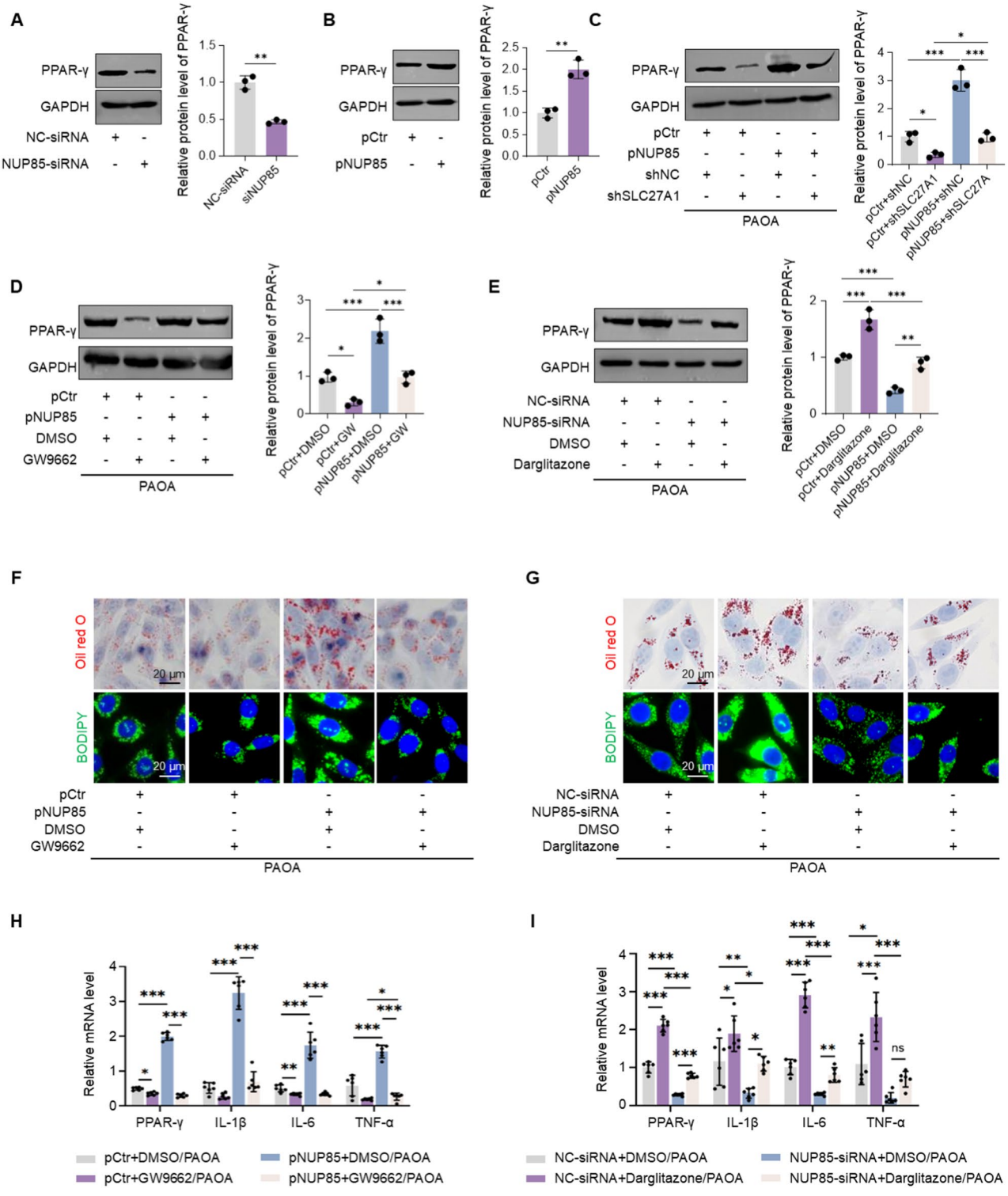


Fig. 6 (See legend on next page.)

deposition in MASLD-affected livers, and alleviate disease progression in these mice. This research also offers new strategies for the treatment of MASLD.

The expression level of NUP85 is significantly elevated in tumor tissues, exhibiting high expression characteristics in pancreatic cancer, lung cancer, melanoma, and gastrointestinal tumors. Its deficiency can inhibit tumor growth and macrophage infiltration [26, 27]. Clinical studies have identified NUP85 as an independent prognostic factor for prostate cancer, with high

(See figure on previous page.)

Fig. 6 NUP85 regulates lipid deposition and inflammatory response through the PPAR-γ signaling pathway. **(A)** Western blot detects the expression of PPAR-γ protein following transfection with *NUP85*-siRNA. **(B)** Western blot detects the expression of PPAR-γ protein following transfection with pcDNA3.1–3×Flag-NUP85. **(C)** Western blot detects the expression of PPAR-γ protein after the simultaneous transfection of pcDNA3.1–3×Flag-*NUP85* and *SLC27A1*-shRNA. **(D)** Western blot detects the expression of PPAR-γ protein in HepG2 cells following treatment with the PPAR-γ inhibitor GW9662. **(E)** Western blot detects the expression of PPAR-γ protein in HepG2 cells following treatment with the PPAR-γ agonist Darglitazone. **(F)** BODIPY and Oil Red staining detect intracellular lipid droplets following transfection with pcDNA3.1–3×Flag-*NUP85* and treatment with the PPAR-γ inhibitor GW9662. Scale bar, 20 μm. **(G)** BODIPY and Oil Red O staining detect intracellular lipid droplets following transfection with *NUP85*-siRNA and treatment with the PPAR-γ agonist Darglitazone. Scale bar, 20 μm. **(H)** qRT-PCR detects the expression of *PPAR-γ*, *IL1β*, *IL-6*, *and TNF-α* following transfection of pcDNA3.1–3×Flag-*NUP85* and treatment with the PPAR-γ inhibitor GW9662 ($n=6$). **(I)** qRT-PCR detects the expression of *PPAR-γ*, *IL1β*, *IL-6 and TNF-α* following transfection with *NUP85*-siRNA and simultaneous treatment with the PPAR-γ agonist Darglitazone ($n=6$). All data are expressed as the mean ± SD. ns: no significance; * $P<0.05$; ** $P<0.01$; *** $P<0.001$

expression significantly associated with disease progression and poor prognosis [28]. Furthermore, the elevated expression of NUP85 in hepatocellular carcinoma correlates with poor prognosis and is associated with various immune cells and therapeutic agents, thereby establishing it as a potential biomarker for the diagnosis, treatment, and prognosis of hepatocellular carcinoma [29]. MASLD is the most prevalent chronic liver disease worldwide, affecting over 30% of adults [30]. Unfortunately, there are currently no available tools for timely diagnosis [31]. Consequently, there is an urgent need for accurate non-invasive biomarkers for the early diagnosis of MASLD. Initially, we identified through MASLD-related public transcriptome databases that the mRNA expression level of NUP85 was elevated in the livers of patients with NAFL and NASH. Subsequently, we analyzed the peripheral blood serum of patients with MASH and cirrhosis and discovered that, compared to healthy individuals, the expression of NUP85 in the serum of patients was significantly increased, with levels rising progressively as the disease advanced. Notably, the diagnostic performance of NUP85 was found to be significantly superior to that of traditional fatty liver markers, namely ALT, AST, TC, and TG. The combined use of NUP85 with traditional markers has the potential to further enhance the specificity and sensitivity of diagnosis. Our diagnostic method is also safer and more acceptable to patients compared to liver biopsy [32]. In contrast to imaging examinations, serum diagnostics are not influenced by the physician's experience and demonstrate greater sensitivity and specificity for MASLD [33]. In summary, our study reveals for the first time that NUP85 holds significant promise as a diagnostic marker for MASLD, potentially facilitating the early diagnosis of this condition.

Wu et al. [14] confirmed that the expression level of NUP85 increased in the MCD-induced mouse model, alongside significant elevations in lipid deposition and inflammation. In this study, we employed two classic diet-induced MASLD models: HFD-induced mice and MCD-induced mice. These models are currently recognized as effective simulations of human MASLD. Notably, the HFD diet-induced model exhibits a pathogenesis more akin to that observed in humans [34]. The results indicated that, compared to control mice, the expression of NUP85 in the livers of both model groups was elevated. Furthermore, the expression level of NUP85 in the liver tissue of patients was significantly higher than that in healthy individuals. Additionally, we utilized three cell lines to assess the impact of lipid deposition on NUP85 expression. The findings demonstrated that NUP85 expression was up-regulated in PAOA-treated MPH, HepG2, and AML12 cells. Lastly, NUP85 plays a crucial role in promoting lipid deposition, inflammation, and oxidative stress in hepatocytes. These results provide compelling evidence for the association between NUP85 and hepatocyte lipid deposition and inflammation, as well as the progression of MASLD.

The pathogenesis of Metabolic Associated Steatotic Liver Disease (MASLD) involves a multifactorial interaction encompassing lipid metabolism disorders, insulin resistance, inflammatory responses, oxidative stress, dysbiosis of intestinal flora, and genetic susceptibility, thereby forming a complex regulatory network with multiple pathways. These pathways primarily include the lipid metabolism pathway (PPARs/SREBP-1c/DGAT2), insulin signaling pathway (IRS/PI3K/AKT), inflammation and immunity pathway (NF-κB/NLRP3/TLR4), oxidative stress pathway (Nrf2/ROS), fibrosis pathway (TGF-β/Smad/PDGF), and autophagy-lysosomal pathway (AMPK/mTOR/LC3). Lipid metabolism disorders serve as the primary drivers of hepatic fat accumulation; insulin resistance acts as the 'common soil' for MASLD; inflammation and immune activation represent critical transitions from simple steatosis to Metabolic Associated Steatohepatitis (MASH); oxidative stress and mitochondrial damage constitute the 'second strike'; fibrosis progression involves the activation of hepatic stellate cells (HSC) and extracellular matrix (ECM) deposition; and the gut-hepatic axis plays a regulatory role through bacterial metabolites [35]– [36]. In the present study, we discovered that NUP85 enhances the expression of SLC27A1, thereby promoting fatty acid uptake in hepatocytes, which leads to exacerbated hepatic lipid deposition and, consequently, metabolic disorders.Reports indicate that NUP85 interacts with CC motif chemokine receptor 2 (CCR2) and may serve as a significant

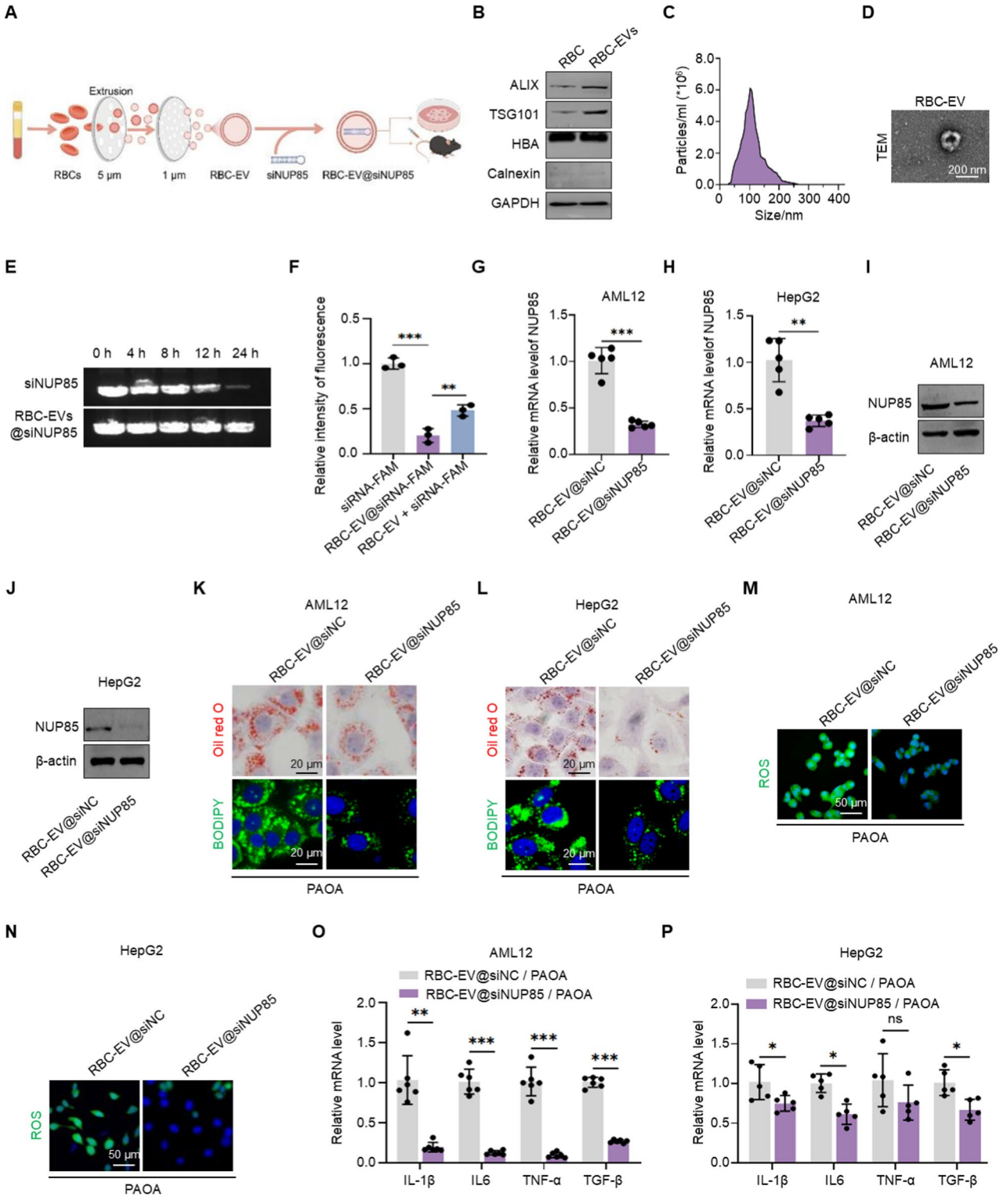


Fig. 7 (See legend on next page.)

regulator of MASLD [9, 14, 37]. However, limited studies have elucidated the regulatory role of NUP85 concerning other key molecules involved in the progression of MASLD. Utilizing the STRING database, we predicted that NUP85 might interact with SLC27A1. Molecular docking experiments corroborated this prediction, and immunoprecipitation experiments further confirmed the interaction between NUP85 and SLC27A1.

(See figure on previous page.)

Fig. 7 RBC-EVs@siNUP85 inhibits PAOA-induced hepatocyte steatosis and inflammation. **(A)** Schematic diagram of RBC-EVs preparation. **(B)** Western blot detects the marker proteins ALIX, TSG101, HBA and Calnexin of RBC and RBC-EVs. **(C)** Analysis of RBC-EVs average size distribution by nanoparticle tracking analysis (NTA). **(D)** Representative TEM image of RBC-EVs. Scale bar, 200 nm. **(E)** Serum stability of free si*Nup85* and RBC-EVs@si*Nup85* by gel electrophoresis analysis. **(F)** Detection of relative fluorescence intensity to analyse the efficiency of si*Nup85* electroporation for RBC-EV introduction. **G-H.** qRT-PCR detected *Nup85* mRNA expression after RBC-EVs@siNC and RBC-EVs@si*Nup85* treated AML12 cells (G) and HepG2 cells (H) respectively. ($n=5$). **I-J.** Western blot detected NUP85 protein expression after RBC-EVs@NC and RBC-EVs@si*Nup85* treated AML12 cells (I) and HepG2 cells (J). **K-L.** Oil red O staining and BODIPY staining detected intracellular lipid droplets after RBC-EVs@siNC and RBC-EVs@si*Nup85* treatment of AML12 cells (K) and HepG2 cells (L) after induction with 1 mM PAOA. Scale bar, 20 μm. **M-N.** Detection of ROS levels after RBC-EVs@siNC and RBC-EVs@si*Nup85* treatment of AML12 cells (M) and HepG2 cells (N) after induction with 1 mM PAOA. Scale bar, 50 μm. **O-P.** qRT-PCR detection of *Il-1β*, *Il6*, *Tnf-α and Tgf-β* levels after RBC-EVs@siNC and RBC-EVs@si*Nup85* treatment of AML12 cells (O) ($n=6$) and HepG2 cells (P) ($n=5$) after induction with 1 mM PAOA. All data are expressed as the mean ± SD. ns: no significance; * $P<0.05$; ** $P<0.01$; *** $P<0.001$

In conclusion, our findings demonstrate that NUP85 interacts with SLC27A1 and enhances its expression, providing new insights into the potential role of NUP85 in lipid metabolism. This protein is crucial for maintaining lipid homeostasis by promoting the uptake and utilization of fatty acids across various metabolic pathways [38]. Solute carrier family is implicated in the PPAR-γ signaling pathway, and SLC27A1 is a key node in the PPAR-γ pathway [39]. PPAR-γ is a major regulator of adipogenesis and lipid metabolism, binding to peroxisome proliferator response elements (PPREs) in the promoter regions of target genes, including SLC27A1, to enhance their transcription [40, 41]. It was shown that activation of PPAR-γ by ligands such as rosiglitazone (a thiazolidinedione) increases SLC27A1 expression in adipocytes and other cell types. This upregulation promotes the uptake and esterification of long-chain fatty acids, leading to lipid accumulation [42]. Like other nuclear receptors, PPAR-γ has multiple functional domains. The N-terminal A/B domain contains the AF-1 region, which influences PPAR-γ's transcriptional activity through autophosphorylation, subsequently affecting the receptor's binding and activation by ligands. The highly conserved DNA-binding region (C region) is responsible for binding to specific DNA sequences in the promoter region of target genes. The C-terminal region, known as the hormone-binding region (E region) or ligand-binding domain (LBD), is the site for ligand binding, such as fatty acids. This binding induces conformational changes in PPAR-γ, thereby activating the receptor. Fatty acids enter the cell via passive diffusion or through membrane transport proteins. Upon entering the cell via passive diffusion or through membrane transport proteins, fatty acids bind to the ligand-binding domain (LBD) of peroxisome proliferator-activated receptor gamma (PPAR-γ). The LBD, characterized as a "ligand pocket," consists of 12 α-helices, wherein the fatty acids are embedded. Through hydrophobic interactions and hydrogen bonding between specific amino acid residues and fatty acids, a conformational rearrangement of helix 12 (H12) occurs, resulting in the formation of the "activated conformation." In conclusion, SLC27A1 facilitates the activation of PPAR-γ by enhancing intracellular fatty acid uptake. Elevated levels of fatty acids, which serve as natural ligands for PPAR-γ, bind to and activate this receptor, thereby enhancing its transcriptional activity [43]. This feedback loop can further amplify the expression of PPAR-γ target genes, including those involved in lipid metabolism. In this context, SLC27A1 functions as an upstream regulator by modulating fatty acid supply, which subsequently influences PPAR-γ activity. The activation of PPAR-γ regulates the expression of a diverse array of target genes, which in turn exert significant physiological functions [44, 45]. In the liver, PPAR-γ upregulates the expression of adipogenic genes such as fatty acid synthase (FASN) and acetyl-CoA carboxylase (ACC), promoting lipid accumulation [46]. Additionally, PPAR-γ induces the expression of CD36/FAT and fatty acid-binding protein 2 (FABP2), thereby facilitating the influx of free fatty acids into hepatocytes [47]. In hepatocytes, the lipogenic effects of PPAR-γ predispose the liver to lipid accumulation. Research conducted by Wei et al. [48] has established that activation of PPAR-γ can lead to lipid accumulation, inflammation, and fibrosis in the livers of MASLD mice. Additionally, another study indicated that targeting PPAR-γ and RXR-α can inhibit lipogenesis and lipid storage in the livers of MASLD zebrafish [49]. Studies have demonstrated that the protective effects of PPAR-γ agonists against NASH/MASH are primarily attributed to their capacity to enhance lipid distribution and insulin sensitivity within adipose tissue [50]. Additionally, these agonists regulate hepatic stellate cells and macrophages, thereby exerting anti-inflammatory and anti-fibrotic effects [51, 52]. In hepatocytes, PPAR-γ functions as a master regulator of lipogenesis; however, its overactivation can lead to hepatic steatosis and lipotoxicity [53]. Our study found that siNUP85 could inhibit lipid deposition in mouse hepatocytes by downregulating PPAR-γ expression. Therefore, we speculate that the role of PPAR-γ in liver injury repair is cell type-specific. This study reveals, for the first time, that NUP85 activates the PPAR-γ signaling pathway by enhancing the expression of SLC27A1, thereby exacerbating liver lipid deposition and inflammatory responses, which promotes the progression of MASLD. This finding provides a novel perspective on the regulatory mechanisms underlying MASLD.

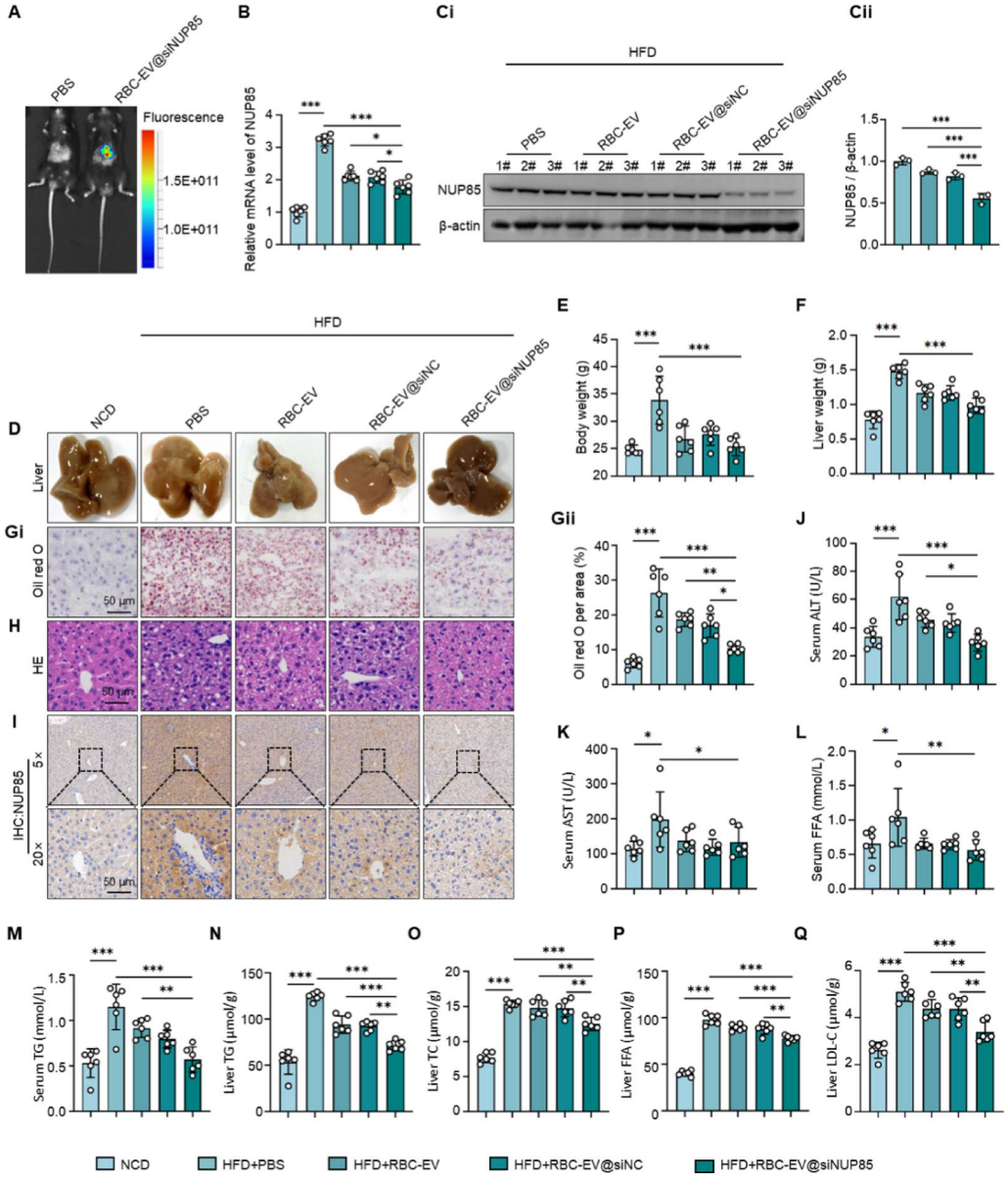


Fig. 8 RBC-EVs@si*Nup85* alleviates liver damage in MASLD mice. **(A)** Biodistribution of Dir-labeled RBC-EVs@si*Nup85* in high-fat diet (HFD) fed mice. **(B)** Changes in *Nup85* mRNA expression in the liver tissue of normal chow diet (NCD) fed mice and HFD-fed mice injected with PBS, RBC-EVs, RBC-EVs@siNC and RBC-EVs@si*Nup85* via the tail vein ($n=6$). **(C)** Western blot detects the NUP85 protein expression in the liver tissue of HFD-fed mice injected with PBS, RBC-EVs, RBC-EVs@siNC and RBC-EVs@si*Nup85* through the tail vein ($n=3$). **D-I.** Liver appearance (D), body weight (E), liver weight (F), liver tissue Oil red O staining (G), liver tissue HE staining (H) and liver tissue NUP85 immunohistochemical staining (I) of NCD-fed mice and HFD-fed mice injected with PBS, RBC-EVs, RBC-EVs@siNC and RBC-EVs@si*Nup85*. ($n=6$). Scale bar, 50 μm. **J-M.** Serum ALT (J), AST (K), FFA (L) and TG (M) levels of NCD-fed mice and HFD-fed mice injected with PBS, RBC-EVs, RBC-EVs@siNC and RBC-EVs@si*Nup85* ($n=6$). **N-Q.** Liver tissue TG (N), TC (O), FFA (P) and LDL-C (Q) levels of NCD-fed mice and HFD-fed mice injected with PBS, RBC-EVs, RBC-EVs@siNC and RBC-EVs@si*Nup85* ($n=6$). All data are expressed as the mean ± SD. ns: no significance; * $P<0.05$; ** $P<0.01$; *** $P<0.001$

The treatment of MASLD presents a significant public health challenge [54]. Previous studies have confirmed that NUP85 plays a critical role in the progression of MASLD. It has been demonstrated that the trans isomer (ISRIB) serves as an inhibitor of NUP85 and can alleviate MASLD [14]. However, the ability of this inhibitor to specifically target NUP85 expression in hepatocytes remains to be investigated, and its biological safety is still uncertain. Currently, five siRNA drugs have received approval from the US Food and Drug Administration (FDA) and the European Commission (EC). These approved siRNA drugs can effectively deliver siRNA to the liver, thereby treating liver-related diseases [55]. Based on prior research, we reaffirm that NUP85 is

instrumental in the progression of MASLD. Consequently, we propose a strategy to mitigate MASLD by inhibiting hepatic NUP85 expression through the delivery of siNUP85. Targeted delivery of siRNA necessitates a safe and efficient delivery carrier, highlighting the importance of developing an effective and safe delivery method for the application of RNA therapeutics. Delivery vectors facilitate the transport of siRNA to target sites. The ideal siRNA delivery vector must protect siRNA from degradation and effectively penetrate target tissues and cells without eliciting harmful immune responses or other adverse effects [56]. Current siRNA delivery systems primarily include viral vectors, lipid nanoparticles (LNPs), extracellular vesicles (EVs), and various nanomaterials-based platforms [57, 58]. Viral vectors are among the most extensively studied RNA delivery systems, with adeno-associated virus (AAV), adenovirus (AdV), herpes simplex virus (HSV), retroviruses, and lentiviruses being the most commonly utilized [59]. Although these vectors demonstrate high transfection efficiency, they also present several limitations. Viral vectors often provoke significant immune responses, resulting in systemic inflammation and diminished therapeutic efficacy upon repeated administration [60]. Furthermore, while adenoviruses can efficiently enter cells via natural receptor interactions, their biodistribution tends to be non-specific. LNPs are lipid vesicles characterized by a homogeneous lipid core, widely employed for the delivery of small molecules and nucleic acids. The LNP delivery systems, noted for their excellent biocompatibility, biodegradability, and ease of large-scale preparation, serve as suitable carriers for siRNA drug delivery. Surface modifications can further enhance LNPs' ability to achieve targeted delivery and improve efficiency [61]. However, high doses of LNPs may induce hepatotoxicity, particularly in formulations containing cationic lipids; multivalent cationic lipids exhibit greater potency than monovalent cationic lipids but are also associated with significantly increased cellular toxicity [62, 63]. Although LNPs offer a novel approach for hepatocyte-targeted therapy in MASLD, numerous challenges persist, as hepatocytes lack specific surface receptors that facilitate nanoparticle targeting [64]. The ApoE-LDLR/VLDLR pathway significantly enhances the endocytosis of siRNA-laden lipid nanoparticles (LNPs) into primary hepatocytes. This mechanism underlies the uptake of Patisiran, the first FDA-approved siRNA-based drug for hepatocytes [19, 65]. Due to the non-specific adsorption by the plasma protein canopy, lipid nanoparticles (LNPs) are inherently captured and accumulated by the mononuclear phagocyte system (MPS), which includes the liver and spleen, following intravenous injection [66]. Furthermore, the heterogeneity of Metabolic Dysfunction-associated Steatotic Liver Disease (MASLD) impacts the composition of the protein canopy and receptor levels, particularly under conditions of tissue hypoxia, potentially influencing the biological fate of LNPs [67]. Extracellular vesicles (EVs) have emerged as a promising RNA delivery system owing to their natural ability to encapsulate and protect RNA molecules for targeted delivery to specific cells. Their biocompatibility and inherent targeting capabilities render them particularly attractive for therapeutic applications, especially in the efficient delivery of RNA-based therapeutics [68, 69]. However, EVs present several challenges, including heterogeneity, difficulties in large-scale production, and inconsistent RNA loading and targeting specificity. In contrast, red blood cell-derived extracellular vesicles (RBC-EVs) may exhibit non-immunogenic properties through blood type matching, allowing them to effectively evade immune surveillance, unlike lentiviruses, adenoviruses, adeno-associated viruses, nanoparticles, and most synthetic transfection reagents. Studies have confirmed that RBC-EVs show no evidence of systemic toxicity or inflammatory effects at therapeutically effective doses, providing a safe and effective strategy for siRNA drug delivery. Blood can be easily obtained from existing blood banks or even from the patient's own blood, with each blood unit containing a substantial number of red blood cells. This approach eliminates the need to expand the cells in culture or the associated risk of mutation accumulation in vitro. The clinical translation of RBC-EV-based therapies could be more effectively achieved using autologous or allogeneic RBC-EVs, akin to human blood transfusions [22]. RBC-EVs naturally tend to accumulate in the liver, and the hepatic accumulation of drug-loaded RBC-EVs results in elevated drug concentrations within this organ, thereby enhancing the therapeutic efficacy of the drug and ensuring unique biosafety [70]. It is crucial to note that since RBC-EVs may carry erythrocyte surface antigens, the intravenous administration of these vesicles could lead to hemolysis if blood group mismatches occur. Consequently, we recommend the use of RBC-EVs derived from autologous or compatible blood groups for human treatments [21]. Furthermore, further development of RBC-EVs coated with targeted peptides or antibodies is essential, as this approach may facilitate the specific delivery of therapeutic RNA to human cells while minimizing adverse side effects in normal tissues [71]. Several studies have successfully developed a method to load siRNA into extracellular vesicles (EVs) using electroporation technology, achieving stable gene knockdown without inducing cell toxicity. This indicates that EVs possess the potential to serve as a new generation of drug carriers, paving the way for the development of safe and effective gene therapies [72, 73]. However, EV-based drug delivery methods are still in their early stages, primarily due to challenges associated with EV isolation, characterization, and content

heterogeneity. In this study, we employed RBC-EVs as the delivery vehicle for siNUP85. The advantages of using RBC-EVs include their broad availability, ease of isolation, non-immunogenicity, and non-carcinogenicity [74]. Our results demonstrate that RBC-EVs carrying si*Nup85* (RBC-EVs@si*Nup85*) can be effectively taken up by hepatocytes without causing noticeable cytotoxicity, leading to a significant inhibition of intracellular NUP85 expression and a reduction in lipid deposition and inflammation in lipotoxic hepatocytes. Furthermore, RBC-EVs loaded with si*Nup85* were administered via tail vein injection in mice. Our findings indicate that RBC-EV@siNUP85 does not significantly affect body weight, liver weight, or serum liver function when compared to the RBC-EV or RBC-EV@siNC groups, suggesting potential off-target effects. We hypothesize that the dosage, route, and timing of RBC-EV@siNup85 injections in mice require further optimization. Additionally, the stability of RBC-EV@siNup85 distribution in vivo and its specificity for localization in hepatocytes within liver tissue necessitate further investigation. These factors may contribute to the observed off-target effects in the control groups (RBC-EV and RBC-EV@siNC). However, our comparative analysis demonstrated no statistically significant differences between the RBC-EV and RBC-EV@siNC control groups across all evaluated parameters, including hepatic histopathology, serum biochemical markers, and NUP85 expression levels. In contrast, the RBC-EV@siNup85 group exhibited reduced NUP85 expression in liver tissue, along with significantly decreased areas of lipid droplets and levels of TG, TC, FFA, and LDL-C in liver tissue compared to RBC-EV@siNC. These results suggest that RBC-EV@siNup85 can significantly inhibit lipid deposition in hepatocytes and promote the repair of liver function. Collectively, our findings indicate the substantial potential of this approach for the treatment of metabolic associated steatotic liver disease (MASLD).

While this study provides valuable insights, it is essential to acknowledge its limitations. A limitation to the study is that our investigation into the mechanism of action of NUP85 was limited to in vitro experiments. Future studies should validate the binding of NUP85 in liver-specific NUP85 knockout mice and restore SLC27A1 function through AAV-NUP85 rescue assays. Additionally, constructing SLC27A1 deletion mutants for validation will further elucidate the key mechanisms of NUP85 action. Secondly, the diagnostic value of NUP85 requires validation with a larger sample size, and it is crucial to collect serum from patients at various disease stages to assess changes in disease progression. A limitation to the generalisability of the study is that it did not consider gender/sex issues. Thirdly, although RBC-EVs serve as a delivery vehicle, the biosafety concerns related to the preparation of blood samples necessitate additional scrutiny. Furthermore, we must explore the long-term biosafety of RBC-EVs for clinical translation. Finally, actively searching for inhibitors of NUP85 represents a promising avenue for future research.

In conclusion, our study demonstrates that NUP85 can activate the PPAR-γ signaling pathway through its interaction with SLC27A1, which exacerbates lipid deposition and inflammatory responses in hepatocytes, thereby promoting the progression of MASLD. Furthermore, NUP85 presents potential as a specific target for the early diagnosis and treatment of MASLD/MASH.

Conclusions

NUP85 levels are elevated in the serum of patients with Metabolic Associated Steatotic Liver Disease (MASLD), demonstrating significant diagnostic efficacy. Furthermore, the delivery of si*Nup85* via red blood cell-derived extracellular vesicles (RBC-EVs) can alleviate the progression of MASLD. Excessive lipid accumulation in the livers of mice subjected to a high-fat diet (HFD) and a methionine-choline deficient diet (MCD), as well as in lipotoxic hepatocytes, leads to the upregulation of NUP85 expression. Consequently, NUP85 activates the PPAR-γ signaling pathway through its interaction with SLC27A1, thereby promoting lipid accumulation and inflammation in hepatocytes.

Abbreviations

MASLD	Metabolic dysfunction-associated steatotic liver disease
MASH	Metabolic dysfunction-associated steatohepatitis
NUP85	Nucleoporin 85
NUPs	Nucleoporins
SLC27A1	Solute carrier family 27 member 1
RBC-EVs	Red blood cell-derived extracellular vesicles
TG	Triglyceride
TC	Total cholesterol
ALT	Alanine aminotransferase
AST	Aspartate aminotransferase
OA	Oleic acid
PA	Palmitic acid
HFD	High-Fat diet
MCD	Methionine-choline-deficient diet
PPAR-γ	Peroxisome proliferator-activated receptor gamma
CCK8	Cell counting kit-8
TEM	Transmission electron microscope
NTA	Nanoparticle tracking analysis
qRT-PCR	Reverse transcription-quantitative PCR
PBS	Phosphate buffered saline
MPH	Mouse primary hepatocytes
FFA	Free fatty acids
Co-IP	Co-immunoprecipitation

Supplementary Information

The online version contains supplementary material available at https://doi.org/10.1186/s12951-025-03900-2.

Supplementary Material 1: Figure S1. Immunohistochemistry and immunofluorescence staining of tissue sections. Figure S2. Immunohistochemical staining of human tissue samples. Figure S3. SLC27A1 promotes lipid deposition in hepatocytes. Figure S4. HepG2 cells were treated with PPAR-γ pathway inhibitors and agonists. Figure S5. RBC-EVs internalization experiment and cell viability detection.Figure S6. Biosafety of RBC-EV@

siNUP85. Figure S7. RBC-EV@siNUP85 inhibits NUP85 expression in liver tissue of HFD mice. Figure S8. RBC-EV@siNUP85 specifically targets NUP85 expression in hepatocytes.

Supplementary Material 2: NUP85 overexpression plasmid (pcDNA3.1-3×Flag-C-pNUP85) sequence information.

Supplementary Material 3: Figure S9. The effect of NUP85 expression on cell viability. Figure S10. The serum NUP85 content of patients with liver cirrhosis. Figure S11. Changes in food intake from mice in the indicated groups. Figure S12. RBC-EVs@siNup85 alleviate inflammation and fibrosis damage in MASLD mice. Table S1. Base characteristics of patients with biopsy-proven MASH. Table S2. Base characteristics of patients with biopsy-proven Cirrhosis.

Acknowledgements
Not applicable.

Author contributions
Z.Z. and SH.L. performed the Investigation and Writing Draft. Y.Z., RZ.X., J.Z. and YN.W. performed Software and Methodology. YM.Y. for conceptualization, funding acquisition, and supervision.

Funding
This work was supported by the National Natural Science Foundation of China (Grant number 82272421, 82570746), Scientific Research Project of Jiangsu Commission of Health (Grant number K2024037), Changzhou's 14th five-year plan project to train high-level health professionals (Grant number 2022CZLJ027), Changzhou Special Program for the Introduction of Foreign Talents (Grant number CQ20240052), Open project of Jiangsu Provincial Key Laboratory of Key Laboratory of Laboratory Medicine (Grant number JSKLM-Z-2024-001, JSKLM-T-2025-01).

Data availability
No datasets were generated or analysed during the current study.

Declarations

Ethics approval and consent to participate
All animal experiments conducted in this study received approval from the Laboratory Animal Management and Ethics Committee of Jiangsu University (Approval Number: UJS-IACUC-AP-2022031502) and adhered strictly to the following international guidelines: the World Medical Association (WMA)"Declaration on the Use of Animals in Biomedical Research," the 3R principles (Replacement, Reduction, Refinement) outlined in the EU Directive 2010/63/EU, and the Chinese national standard "Guidelines for Ethical Review of Laboratory Animal Welfare." The patient samples/data and healthy donor samples/data collection used in this study were approved by the Research Ethics Committee of the Affiliated Wujin Hospital of Jiangsu University (Approval No: 2025-SR-019), and complied with the ethical guidelines of the Declaration of Helsinki. The acquisition of tissues used in this study conformed to the World Health Organization's Guiding Principles on Human Cell, Tissue, and Organ Transplantation. The risks posed by the study to the subjects are minimal, and waiving informed consent will not adversely affect their rights or health. This study does not utilize medical records or specimens that patients or subjects have explicitly declined to use previously. It is explicitly stated that no privacy or personal identity information of the subjects will be collected during the research process, and stringent measures are in place to ensure that such information remains confidential. The specimens involved in the clinical trials of diagnostic reagents consist of residual samples or specimens from a biobank, which have been used for medical diagnosis and treatment. These specimens have had all personal and identifiable information removed and are identified solely by codes.

Consent to for publication
Not applicable.

Competing interests
The authors declare no competing interests.

Author details
[1]Department of Laboratory Medicine, Wujin Hospital Affiliated with Jiangsu University, Jiangsu University, Changzhou 213017, China
[2]Department of Laboratory Medicine, School of Medicine, Jiangsu University, Zhenjiang 212013, China
[3]Changzhou Key Laboratory of Exosome Foundation and Transformation Application, Wujin Hospital Affiliated with Jiangsu University (Wujin Clinical College of Xuzhou Medical University), Changzhou 213017, China
[4]The Affiliated Suzhou Hospital of Nanjing Medical University, Suzhou Municipal Hospital, Gusu School, Nanjing Medical University, Suzhou, China

Received: 16 September 2025 / Accepted: 26 November 2025
Published online: 18 December 2025

References

1. Pang Z, Zhang H, Zheng S, Yang X, Liu C, Han Q, et al. HNF4α-CDKL3 axis restricts MASLD progression by targeting FoxO1 via noncanonical phosphorylation. Hepatology. 2024. https://doi.org/10.1097/HEP.0000000000001147.
2. Long MT, Noureddin M, Lim JK. AGA clinical practice update: diagnosis and management of nonalcoholic fatty liver disease in lean individuals. Expert Rev Gastroenterol. 2022;163(3):764–74. https://doi.org/10.1053/j.gastro.2022.06.023.
3. Wan Z, Liu X, Yang X, Huang Z, Chen X, Feng Q, et al. MicroRNA-411-5p alleviates lipid deposition in metabolic dysfunction-associated steatotic liver disease by targeting the EIF4G2/FOXO3 axis. Cell Mol Life Sci. 2024;81(1):398. https://doi.org/10.1007/s00018-024-05434-6.
4. Polyzos SA, Targher G. Hepatic thyroid hormone receptor-β signalling: mechanisms and recent advancements in the treatment of metabolic dysfunction-associated steatohepatitis. Diabetes Obes Metab. 2024. https://doi.org/10.1111/dom.16117.
5. Zhou JH, Cai JJ, She ZG, Li HL. Noninvasive evaluation of nonalcoholic fatty liver disease: current evidence and practice. World J Gastroenterol. 2019;25(11):1307–26. https://doi.org/10.3748/wjg.v25.i11.1307.
6. Ravindran E, Lesca G, Januel L, Goldgruber L, Dickmanns A, Margot H, et al. Case report: compound heterozygous NUP85 variants cause autosomal recessive primary microcephaly. Front Neurol. 2023;14:1124886. https://doi.org/10.3389/fneur.2023.1124886.
7. Beck M, Hurt E. The nuclear pore complex: understanding its function through structural insight. Nat Rev Mol Cell Biol. 2017;18(2):73–89. https://doi.org/10.1038/nrm.2016.147.
8. Li KM, Meng LF, Yang ZH, Hu WT. NUP155 and NDC1 interaction in NSCLC: a promising target for tumor progression. Front Pharmacol. 2024;15:1514367. https://doi.org/10.3389/fphar.2024.1514367.
9. Terashima Y, Toda E, Itakura M, Otsuji M, Yoshinaga S, Okumura K, et al. Targeting FROUNT with disulfiram suppresses macrophage accumulation and its tumor-promoting properties. Nat Commun. 2020;11(1):609. https://doi.org/10.1038/s41467-020-14338-5.
10. Zhang M, Tian SY, Ma SY, Zhou X, Zheng XH, Li B, et al. <article-title update="added">Deficient <scp>chaperone-mediated</scp>autophagy in macrophage aggravates inflammation of nonalcoholic steatohepatitis by targeting Nup85. Liver Int. 2023;43(5):1021–34. https://doi.org/10.1111/liv.15547.
11. Yang K, Yu X, Guo Z, Fang Z, Zhang H, Zhang W, et al. PIM1 alleviated liver oxidative stress and NAFLD by regulating the NRF2/HO-1/NQO1 pathway. Life Sci. 2024;122714. https://doi.org/10.1016/j.lfs.2024.122714.
12. He J, Qian YC, Yin YC, Kang JR, Pan TR. Polydatin: a potential NAFLD therapeutic drug that regulates mitochondrial autophagy through SIRT3-FOXO3-BNIP3 and PINK1-PRKN mechanisms-a network pharmacology and experimental investigation. Chem Biol Interact. 2024;111110. https://doi.org/10.1016/j.cbi.2024.111110.
13. Xiao MC, Jiang N, Chen LL, Liu F, Liu SQ, Ding CH, et al. TRIB3-TRIM8 complex drives NAFLD progression by regulating HNF4α stability. J Hepatol. 2024. https://doi.org/10.1016/j.jhep.2023.12.029.
14. Wu YC, Yan Q, Yue SQ, Pan LX, Yang DS, Tao LS, et al. NUP85 alleviates lipid metabolism and inflammation by regulating PI3K/AKT signaling pathway in nonalcoholic fatty liver disease. Int J Biol Sci. 2024;20(6):2219–35. https://doi.org/10.7150/ijbs.92337.

15. Cao L, Du M, Cai M, Feng Y, Miao J, Sun J, et al. Neutrophil membrane-coated nanoparticles for targeted delivery of toll-like receptor 4 siRNA ameliorate LPS-induced acute lung injury. Int J Pharm. 2024;124960. https://doi.org/10.1016/j.ijpharm.2024.124960.
16. Jogdeo CM, Panja S, Kumari N, Tang W, Kapoor E, Siddhanta K, et al. Inulin-based nanoparticles for targeted siRNA delivery in acute kidney injury. J Control Release. 2024. https://doi.org/10.1016/j.jconrel.2024.10.027.
17. Kalaimani K, Balachandran S, Boopathy LK, Roy A, Jayachandran B, Sankaranarayanan S, et al. Recent advancements in small interfering RNA (siRNA) based therapeutic approach on breast cancer. Eur J Pharmacol. 2024;176877. https://doi.org/10.1016/j.ejphar.2024.176877.
18. Taniuchi K, Yawata T, Tsuboi M, Ueba T, Saibara T. Efficient delivery of small interfering RNAs targeting particular mRNAs into pancreatic cancer cells inhibits invasiveness and metastasis of pancreatic tumors. Oncotarget. 2019;10(30):2869–86. https://doi.org/10.18632/oncotarget.26880.
19. Lyu Y, Yang X, Yang L, Dai J, Qin H, Zhou Y, et al. Lipid nanoparticle-mediated hepatocyte delivery of siRNA and silibinin in metabolic dysfunction-associated steatotic liver disease. J Control Release. 2024. https://doi.org/10.1016/j.jconrel.2024.07.011.
20. Li S, Xiong F, Zhang S, Liu J, Gao G, Xie J, et al. Oligonucleotide therapies for nonalcoholic steatohepatitis. Mol Ther Nucleic Acids. 2024;35(2):102184. https://doi.org/10.1016/j.omtn.2024.102184.
21. Xu L, Xu X, Liang Y, Wen C, Ouyang K, Huang J, et al. Osteoclast-targeted delivery of anti-miRNA oligonucleotides by red blood cell extracellular vesicles. J Control Release. 2023;358:259–72. https://doi.org/10.1016/j.jconrel.2023.04.043.
22. Peng B, Yang Y, Wu Z, Tan R, Pham TT, Yeo EYM, et al. Red blood cell extracellular vesicles deliver therapeutic SiRNAs to skeletal muscles for treatment of cancer cachexia. Mol Ther. 2023;31(5):1418–36. https://doi.org/10.1016/j.ymthe.2023.03.036.
23. Qi R, Feng M, Tan X, Gan L, Yan G, Sun C. FATP1 silence inhibits the differentiation and induces the apoptosis in chicken preadipocytes. Mol Biol Rep. 2013;40(4):2907–14. https://doi.org/10.1007/s11033-012-2306-4.
24. Gavrilova O, Haluzik M, Matsusue K, Cutson JJ, Johnson L, Dietz KR, Nicol CJ, Vinson C, Gonzalez FJ, Reitman ML. Liver peroxisome proliferator-activated receptor gamma contributes to hepatic steatosis, triglyceride clearance, and regulation of body fat mass. J Biol Chem. 2003;278(36):34268–76. https://doi.org/10.1074/jbc.M300043200.
25. Thomas JA, Kendall BJ, Dalais C, Macdonald GA, Thrift AP. Hepatocellular and extrahepatic cancers in non-alcoholic fatty liver disease: a systematic review and meta-analysis. Eur J Cancer. 2022;173:250–62. https://doi.org/10.1016/j.ejca.2022.06.051.
26. Xia R, Tang H, Shen J, Xu S, Liang Y, Zhang Y, et al. Prognostic value of a novel glycolysis-related gene expression signature for gastrointestinal cancer in the Asian population. Cancer Cell Int. 2021;21(1):154. https://doi.org/10.1186/s12935-021-01857-4.
27. Li Y, Zhu J, Zhai F, Kong L, Li H, Jin X. Advances in the understanding of nuclear pore complexes in human diseases. J Cancer Res Clin Oncol. 2024;150(7):374. https://doi.org/10.1007/s00432-024-05881-5.
28. Chen Z, Guan H, Chen L, Yuan X, Sun W, Chen M. Comprehensive pan-cancer evaluation of NUP85 prognosis, immune infiltration response, and validation in prostate cancer. Discov Oncol. 2025;16(1):1953. https://doi.org/10.1007/s12672-025-03735-1.
29. Liu X, Ding Z, Wu H, Ma J, Lu J. [Analysis of correlation between high expression of nucleoporin 85 (NUP85) and immune cell infiltration in hepatocellular carcinoma]. Xi Bao Yu Fen Zi Mian Yi Xue Za Zhi. 2024;40(6):508–19.
30. Miao L, Targher G, Byrne CD, Cao YY, Zheng MH. Current status and future trends of the global burden of MASLD. Trends Endocrinol Metab. 2024;35(8):697–707. https://doi.org/10.1016/j.tem.2024.02.007.
31. Park J, Le AK, Tseng TC, Yeh ML, Jun DW, Trinh H, et al. Progression rates by Age, Sex, Treatment, and disease activity by AASLD and EASL criteria: data for precision medicine. Clin Gastroenterol Hepatology: Official Clin Pract J Am Gastroenterological Association. 2022;20(4):874–e854. https://doi.org/10.1016/j.cgh.2021.05.062.
32. Bedossa P. <article-title update="added">Diagnosis of non-alcoholic fatty liver disease/non-alcoholic steatohepatitis: why liver biopsy is essential. Liver Int. 2018;38(Suppl 1):64–6. https://doi.org/10.1111/liv.13653.
33. Wang J, Jia B, Miao J, Li D, Wang Y, Han L, et al. An novel effective and safe model for the diagnosis of nonalcoholic fatty liver disease in China: gene excavations, clinical validations, and mechanism elucidation. J Transl Med. 2024;22(1):624. https://doi.org/10.1186/s12967-024-05315-3.
34. Liu T, Sui M, Tian M, Wu N, Zhao S, Wang Y et al. Sulfonated albumin from hepatocytes accelerates liver fibrosis in nonalcoholic fatty liver disease through Endoplasmic reticulum stress. Free radical biology & medicine. 2024. https://doi.org/10.1016/j.freeradbiomed.2024.12.055
35. Benedé-Ubieto R, Cubero FJ, Nevzorova YA. Breaking the barriers: the role of gut homeostasis in Metabolic-Associated steatotic liver disease (MASLD). Gut Microbes. 2024;16(1):2331460. https://doi.org/10.1080/19490976.2024.2331460.
36. Musso G, Gambino R, Cassader M. Recent insights into hepatic lipid metabolism in non-alcoholic fatty liver disease (NAFLD). Prog Lipid Res. 2009;48(1):1–26. https://doi.org/10.1016/j.plipres.2008.08.001.
37. Terashima Y, Onai N, Murai M, Enomoto M, Poonpiriya V, Hamada T, et al. Pivotal function for cytoplasmic protein FROUNT in CCR2-mediated monocyte chemotaxis. Nat Immunol. 2005;6(8):827–35. https://doi.org/10.1038/ni1222.
38. Acharya R, Shetty SS, Pavan G, Monteiro F, Munikumar M, Naresh S, et al. AI-based homology modelling of fatty acid transport protein 1 using AlphaFold: structural elucidation and molecular dynamics exploration. Biomolecules. 2023. https://doi.org/10.3390/biom13111670.
39. Jiang Y, Zhou X, He Z, Wei L, Zhu S, Zhang H, et al. DHA Improves neurodevelopmental abnormalities in offspring of gestational diabetes mellitus patients via the PPAR-γ/FATP4 pathway. Biochem Pharmacol. 2024;116726. https://doi.org/10.1016/j.bcp.2024.116726.
40. Mu F, Jing Y, Ning B, Huang J, Cui T, Guo Y, You X, Yan X, Li H, Wang N. Peroxisome proliferator-activated receptor γ isoforms differentially regulate preadipocyte proliferation, apoptosis, and differentiation in chickens. Poult Sci. 2020;99(12):6410–21. https://doi.org/10.1016/j.psj.2020.09.086.
41. Briot A, Decaunes P, Volat F, Belles C, Coupaye M, Ledoux S, et al. Senescence alters PPARγ (Peroxisome Proliferator-Activated receptor Gamma)-dependent fatty acid handling in human adipose tissue microvascular endothelial cells and favors inflammation. Arterioscler Thromb Vasc Biol. 2018;38(5):1134–46. https://doi.org/10.1161/ATVBAHA.118.310797.
42. Blanchard PG, Turcotte V, Côté M, Gélinas Y, Nilsson S, Olivecrona G, Deshaies Y, Festuccia WT. Peroxisome proliferator-activated receptor γ activation favours selective subcutaneous lipid deposition by coordinately regulating lipoprotein lipase modulators, fatty acid transporters and lipogenic enzymes. Acta Physiol (Oxf). 2016;217(3):227–39. https://doi.org/10.1111/apha.12665.
43. Li J, Tian J, Yin H, Peng Y, Liu S, Yao S, et al. Chemical conjugation of FITC to track silica nanoparticles in vivo and in vitro: an emerging method to assess the reproductive toxicity of industrial nanomaterials. Environ Int. 2021;152:106497. https://doi.org/10.1016/j.envint.2021.106497.
44. Itoh T, Fairall L, Amin K, Inaba Y, Szanto A, Balint BL, et al. Structural basis for the activation of PPARgamma by oxidized fatty acids. Nat Struct Mol Biol. 2008;15(9):924–31. https://doi.org/10.1038/nsmb.1474.
45. Chinetti G, Fruchart JC, Staels B. Peroxisome proliferator-activated receptors (PPARs): nuclear receptors at the crossroads between lipid metabolism and inflammation. Inflamm Res. 2000;49(10):497–505. https://doi.org/10.1007/s000110050622.
46. Li X, Zhang H, Yu F, Xie S, Wang T, Zhang R, et al. IRF8 aggravates nonalcoholic fatty liver disease via BMAL1/PPARγ axis. Genes & Diseases. 2025;12(3):101333. https://doi.org/10.1016/j.gendis.2024.101333.
47. Li J, Li C, Wu X, Dong Y, Li Y, Jiao X, et al. Protocatechuic acid suppresses lipid uptake and synthesis through the PPARγ pathway in high-fat diet-induced NAFLD mice. J Agric Food Chem. 2025. https://doi.org/10.1021/acs.jafc.4c01354.
48. Wei J, Luo J, Yang F, Feng X, Zeng M, Dai W, et al. Cultivated *Enterococcus faecium* B6 from children with obesity promotes nonalcoholic fatty liver disease by the bioactive metabolite tyramine. Gut microbes. 2024;16(1):2351620. https://doi.org/10.1080/19490976.2024.2351620.
49. Zhang P, Liu N, Xue M, Zhang M, Xiao Z, Xu C. β-sitosterol reduces the content of triglyceride and cholesterol in a high-fat diet-induced non-alcoholic fatty liver disease zebrafish (*Danio rerio*) model. Animals. 2024;14(9):1289. https://doi.org/10.3390/ani14091289.
50. Ratziu V, Giral P, Jacqueminet S, et al. Rosiglitazone for nonalcoholic steatohepatitis: one-year results of the randomized placebo-controlled fatty liver improvement with Rosiglitazone therapy (FLIRT) trial. Gastroenterology. 2008;135(1):100–10. https://doi.org/10.1053/j.gastro.2008.03.078.
51. Ni XX, Li XY, Wang Q, Hua J. Regulation of peroxisome proliferator-activated receptor-gamma activity affects the hepatic stellate cell activation and the progression of NASH via TGF-β1/Smad signaling pathway. J Physiol Biochem. 2021;77(1):35–45. https://doi.org/10.1007/s13105-020-00777-7.
52. Wu HM, Ni XX, Xu QY, Wang Q, Li XY, Hua J. Regulation of lipid-induced macrophage polarization through modulating peroxisome proliferator-activated

receptor-gamma activity affects hepatic lipid metabolism via a Toll-like receptor 4/NF-κB signaling pathway. J Gastroenterol Hepatol. 2020;35(11):1998–2008. https://doi.org/10.1111/jgh.15025.
53. Newberry EP, Xie Y, Kennedy S, et al. Decreased hepatic triglyceride accumulation and altered fatty acid uptake in mice with deletion of the liver fatty acid-binding protein gene. J Biol Chem. 2003;278(51):51664–72. https://doi.org/10.1074/jbc.M309377200.
54. Cotter TG, Rinella M. Nonalcoholic fatty liver disease 2020: the state of the disease. Gastroenterology. 2020;158(7):1851–64. https://doi.org/10.1053/j.gastro.2020.01.052.
55. Tang Q, Khvorova A. RNAi-based drug design: considerations and future directions. Nat Rev Drug Discov. 2024;23(5):341–64. https://doi.org/10.1038/s41573-024-00912-9.
56. Xiong L, Chen S, Li S, He D, Wang Y, Zhang Q, et al. ATP-responsive tumor targeted lipid nanoparticle for enhanced siRNA delivery and improved treatment efficacy in melanoma. J Control Release. 2025;113622. https://doi.org/10.1016/j.jconrel.2025.113622.
57. Whitehead KA, Langer R, Anderson DG. Knocking down barriers: advances in SiRNA delivery. Nat Rev Drug Discov. 2009;8(2):129–38. https://doi.org/10.1038/nrd2742.
58. Byun J, Wu Y, Park J, Kim JS, Li Q, Choi J, et al. RNA nanomedicine: delivery strategies and applications. AAPS J. 2023;25(6):95. https://doi.org/10.1208/s12248-023-00860-z.
59. Song Z, Tao Y, Liu Y, Li J. Advances in delivery systems for CRISPR/Cas-mediated cancer treatment: a focus on viral vectors and extracellular vesicles. Front Immunol. 2024;15:1444437. https://doi.org/10.3389/fimmu.2024.1444437.
60. Verdera HC, Kuranda K, Mingozzi F. AAV vector immunogenicity in humans: a long journey to successful gene transfer. Mol Ther. 2020;28(3):723–46. https://doi.org/10.1016/j.ymthe.2019.12.010.
61. Cullis PR, Hope MJ. Lipid nanoparticle systems for enabling gene therapies. Mol Ther. 2017;25(7):1467–75. https://doi.org/10.1016/j.ymthe.2017.03.013.
62. Bian X, Zhou L, Luo Z, Liu G, Hang Z, Li H, Li F, Wen Y. Emerging delivery systems for enabling precision nucleic acid therapeutics. ACS Nano. 2025. https://doi.org/10.1021/acsnano.4c11858.
63. Thi TTH, Suys EJA, Lee JS, Nguyen DH, Park KD, Truong NP. Lipid-based nanoparticles in the clinic and clinical trials: from cancer nanomedicine to COVID-19 vaccines. Vaccines (Basel). 2021. https://doi.org/10.3390/vaccines9040359.
64. Kumar V, Xin X, Ma J, Tan C, Osna N, Mahato RI. Therapeutic targets, novel drugs, and delivery systems for diabetes associated NAFLD and liver fibrosis. Adv Drug Deliv Rev. 2021;176:113888. https://doi.org/10.1016/j.addr.2021.113888.
65. Woitok MM, Zoubek ME, Doleschel D, Bartneck M, Mohamed MR, Kießling F, et al. Lipid-encapsulated siRNA for hepatocyte-directed treatment of advanced liver disease. Cell Death Dis. 2020;11(5):343. https://doi.org/10.1038/s41419-020-2571-4.
66. Kim J, Eygeris Y, Ryals RC, Jozić A, Sahay G. Strategies for non-viral vectors targeting organs beyond the liver. Nat Nanotechnol. 2023. https://doi.org/10.1038/s41565-023-01563-4.
67. Shen GM, Zhao YZ, Chen MT, Zhang FL, Liu XL, Wang Y, Liu CZ, Yu J, Zhang JW. Hypoxia-inducible factor-1 (HIF-1) promotes LDL and VLDL uptake through inducing VLDLR under hypoxia. Biochem J. 2012;441(2):675–83. https://doi.org/10.1042/BJ20111377.
68. Barile L, Vassalli G. Exosomes: therapy delivery tools and biomarkers of diseases. Pharmacol Ther. 2017;174:63–78. https://doi.org/10.1016/j.pharmthera.2017.02.020.
69. Spiers HVM, Stadler LKJ, Smith H, Kosmoliaptsis V. Extracellular vesicles as drug delivery systems in organ transplantation: the next frontier. Pharmaceutics. 2023. https://doi.org/10.3390/pharmaceutics15030891.
70. Zhang G, Huang X, Xiu H, Sun Y, Chen J, Cheng G, et al. Extracellular vesicles: natural liver-accumulating drug delivery vehicles for the treatment of liver diseases. J Extracell Vesicles. 2020;10(2):e12030. https://doi.org/10.1002/jev2.12030.
71. Usman WM, Pham TC, Kwok YY, Vu LT, Ma V, Peng B, Chan YS, Wei L, Chin SM, Azad A, He AB, Leung AYH, Yang M, Shyh-Chang N, Cho WC, Shi J, Le MTN. Efficient RNA drug delivery using red blood cell extracellular vesicles. Nat Commun. 2018;9(1):2359. https://doi.org/10.1038/s41467-018-04791-8.
72. Alvarez-Erviti L, Seow Y, Yin H, Betts C, Lakhal S, Wood MJ. Delivery of SiRNA to the mouse brain by systemic injection of targeted exosomes. Nat Biotechnol. 2011;29(4):341–5. https://doi.org/10.1038/nbt.1807.
73. Wahlgren J, De LKT, Brisslert M, Vaziri Sani F, Telemo E, Sunnerhagen P, et al. Plasma exosomes can deliver exogenous short interfering RNA to monocytes and lymphocytes. Nucleic Acids Res. 2012;40(17):e130. https://doi.org/10.1093/nar/gks463.
74. Biagiotti S, Canonico B, Tiboni M, Abbas F, Perla E, Montanari M, et al. Efficient and highly reproducible production of red blood cell-derived extracellular vesicle mimetics for the loading and delivery of RNA molecules. Sci Rep. 2024;14(1):14610. https://doi.org/10.1038/s41598-024-65623-y.

Publisher's note

Springer Nature remains neutral with regard to jurisdictional claims in published maps and institutional affiliations.